AGU PUBLICATIONS

Paleoceanography

RESEARCH ARTICLE
10.1002/2015PA002824

Key Points:
- A new, isotope-enabled version of ROMS is presented
- Mesoscale processes significantly impact coral proxy sites
- Downscaling changes the ENSO-δ^{18}O relation in the central tropical Pacific

Supporting Information:
- Figures S1–S4

Correspondence to:
S. Stevenson,
slgs@hawaii.edu

Citation:
Stevenson, S., B. S. Powell, M. A. Merrifield, K. M. Cobb, J. Nusbaumer, and D. Noone (2015), Characterizing seawater oxygen isotopic variability in a regional ocean modeling framework: Implications for coral proxy records, *Paleoceanography*, *30*, 1573–1593, doi:10.1002/2015PA002824.

Received 27 APR 2015
Accepted 1 NOV 2015
Accepted article online 5 NOV 2015
Published online 30 NOV 2015

Characterizing seawater oxygen isotopic variability in a regional ocean modeling framework: Implications for coral proxy records

S. Stevenson[1,2], B. S. Powell[1], M. A. Merrifield[1], K. M. Cobb[3], J. Nusbaumer[4], and D. Noone[5]

[1]Department of Oceanography, University of Hawaii, Honolulu, Hawaii, USA, [2]Climate and Global Dynamics Division, National Center for Atmospheric Research, Boulder, Colorado, USA, [3]Department of Earth and Atmospheric Sciences, Georgia Institute of Technology, Atlanta, Georgia, USA, [4]Department of Atmospheric and Oceanic Sciences and Cooperative Institute for Research in the Environmental Sciences, University of Colorado Boulder, Boulder, Colorado, USA, [5]College of Earth, Ocean, and Atmospheric Sciences, Oregon State University, Corvallis, Oregon, USA

Abstract Reconstructions of the El Niño–Southern Oscillation (ENSO) are often created using the oxygen isotopic ratio in tropical coral skeletons (δ^{18}O). However, coral δ^{18}O can be difficult to interpret quantitatively, as it reflects changes in both temperature and the δ^{18}O value of seawater. Small-scale (10–100 km) processes affecting local temperature and seawater δ^{18}O are also poorly quantified and contribute an unknown amount to intercoral δ^{18}O offsets. A new version of the Regional Ocean Modeling System capable of directly simulating seawater δ^{18}O (isoROMS) is therefore presented to address these issues. The model is used to simulate δ^{18}O variations over the 1979–2009 period throughout the Pacific at coarse (O(50 km)) resolution, in addition to 10 km downscaling experiments covering the central equatorial Pacific Line Islands, a preferred site for paleo-ENSO reconstruction from corals. A major impact of downscaling at the Line Islands is the ability to resolve fronts associated with tropical instability waves (TIWs), which generate large excursions in both temperature and seawater δ^{18}O at Palmyra Atoll (5.9°N, 162.1°W). TIW-related sea surface temperature gradients are smaller at neighboring Christmas Island (1.9°N, 157.5°W), but the interaction of mesoscale features with the steep island topography nonetheless generates cross-island temperature differences of up to 1°C. These nonlinear processes alter the slope of the salinity:seawater δ^{18}O relationship at Palmyra and Christmas, as well as affect the relation between coral δ^{18}O and indices of ENSO variability. Consideration of the full physical oceanographic context of reef environments is therefore crucial for improving δ^{18}O-based ENSO reconstructions.

1. Introduction

The El Niño–Southern Oscillation (ENSO) dominates interannual variability in the tropical Pacific and affects extreme events throughout the world. ENSO impacts midlatitude stationary wave patterns [*Hoskins and Karoly*, 1981] and the location and intensity of the tropical convergence zones [*Folland et al.*, 2002; *Cai et al.*, 2012], among other influences. However, the observational data available for characterization of ENSO are limited. Gridded data sets are available extending to the early twentieth century but high-quality in situ monitoring dates primarily to the 1980s, with the inception of the Tropical Ocean–Global Atmosphere/Tropical Atmosphere-OceanAO buoy array [*McPhaden et al.*, 1998]. Exacerbating this problem, climate model-based assessments indicate timescales of natural ENSO variability on the order of centuries [*Wittenberg*, 2009; *Stevenson et al.*, 2010, 2012], indicating that the instrumental record undersamples the full range of unforced ENSO changes.

Paleoclimate proxy data are the only option for obtaining information on ENSO variability prior to the start of the instrumental record. Of the many possible sources of paleoclimate information, tropical corals are the best suited for ENSO reconstruction (see review by *Lough* [2010]). Corals grow rapidly, providing seasonal-to-monthly temporal resolution; they are found on equatorial islands close to the ENSO "centers of action," and their geochemistry is strongly influenced by local conditions. The most commonly measured quantity is the isotopic ratio of oxygen in coralline aragonite (δ^{18}O), which records the δ^{18}O value of the surrounding seawater subject to a temperature-dependent fractionation caused by inorganic calcium

carbonate precipitation [*Epstein et al.*, 1953; *Fairbanks et al.*, 1997]. When resources allow, multiproxy studies are employed using coral Sr/Ca, an sea surface temperature (SST)-only proxy [*Beck et al.*, 1992; *Alibert and McCulloch*, 1997], enabling the quantification of the SST and seawater δ^{18}O components of coral δ^{18}O variability [*Nurhati et al.*, 2009, 2011; *DeLong et al.*, 2012; *Cahyarini et al.*, 2008]. Several studies confirm that coral δ^{18}O records from the central tropical Pacific are highly correlated with instrumental indices of ENSO (e.g., the NINO3.4 index) [*Evans et al.*, 1998; *Cobb et al.*, 2001], enabling the extension of the instrumental record of ENSO through the last millennium [*Cobb et al.*, 2003] and portions of the Holocene [*Woodroffe et al.*, 2003; *Cobb et al.*, 2013; *McGregor et al.*, 2013].

To quantify past ENSO variability using coral δ^{18}O, a conversion between δ^{18}O and ENSO-relevant physical variables is required. This is typically done by assuming that seawater δ^{18}O and salinity are linearly proportional [*Thompson et al.*, 2011], an assumption justified by the commonalities between physical processes affecting the two (advection, precipitation, evaporation, diffusion, etc.). However, the uncertainties in such linear "pseudoproxy" relations lead to extremely large errors on the resulting variance estimate [*Stevenson et al.*, 2013], and the dominant source of conversion errors remains poorly quantified. In part, these conversion errors reflect uncertainties in the salinity:seawater δ^{18}O relationship and its variability through time, for which only a handful of observations exist [e.g., *Conroy et al.*, 2014]. This relationship need not necessarily be linear: it is by no means required that horizontal advective or vertical entrainment processes should affect salinity and δ^{18}O proportionately, and thus, including additional physics in a pseudoproxy context might significantly impact the salinity:δ^{18}O relationship. Another issue is scale: pseudoproxy conversions may be missing physical processes operating on spatial scales smaller than the grid sizes of instrumental products used for the linear regression, and the minimum scale of relevant processes remains unknown.

To fully characterize the connection between ENSO and variability near a given reef, it is necessary to examine δ^{18}O variability in a three-dimensional, dynamically consistent framework capable of capturing the significant processes that control δ^{18}O in seawater. Environmental monitoring efforts are underway in many locations, but the available data remain limited. Numerical models can fill in the gaps: previous studies have used isotope-enabled general circulation models (GCMs) to assess δ^{18}O dynamics [*Russon et al.*, 2013], but the biases and coarse resolution of GCMs make direct comparison with δ^{18}O records difficult. In particular, GCMs commonly overestimate the strength of the equatorial trade winds and exhibit a corresponding tendency for erroneously cold temperatures in the east to central Pacific; this is likely associated with overly energetic mixing/upwelling along the equator [*Guilyardi et al.*, 2009; *Bellenger et al.*, 2013]. The Regional Ocean Modeling System (ROMS) [*Shchepetkin and McWilliams*, 2005] avoids these issues, being adaptable to an arbitrarily fine grid and accepting boundary conditions from observational data products. We have incorporated the water isotopologues $H_2^{16}O$ and $H_2^{18}O$ directly into ROMS (hereafter referred to as isoROMS), from which the δ^{18}O value of seawater is calculated: this allows the construction of an approximate isotopic "reanalysis" around any area of interest.

The primary focus of the present study is the central equatorial Pacific Line Islands chain, which has been the focus of many previous coral δ^{18}O collection efforts; Palmyra Atoll [*Cobb et al.*, 2003; *Nurhati et al.*, 2009] and Kiritimati (Christmas) Island [*Evans et al.*, 1999, 2000; *McGregor et al.*, 2011; *Cobb et al.*, 2013] are particularly well studied. These islands lie in a dynamically interesting region affected by the North Equtatorial Countercurrent (NECC) [*Hamann et al.*, 2004] and tropical instability waves (TIWs) [*Legeckis*, 1977; *Kennan and Flament*, 2000; *Lyman et al.*, 2007]. At these latitudes the Rossby deformation radius is quite large (O(200 km)) [*Chelton et al.*, 1998], implying that submesoscale dynamics (operating on scales less than half the deformation radius) can contribute significantly to the kinetic energy budget on the 10–100 km scale [*Marchesiello et al.*, 2011]. The present modeling configuration is ideally suited to assess the effects of resolution on δ^{18}O variability in the Line Islands, and each island is considered here separately.

2. Experimental Setup

2.1. ROMS Configuration

This study employs the Regional Ocean Modeling System (ROMS) [*Shchepetkin and McWilliams*, 2005], a free-surface, terrain-following ocean model which uses a split-explicit time stepping algorithm. ROMS was especially designed for accuracy when simulating small-scale processes and has been used extensively for simulating island environments in the past, including the Hawaiian island chain [*Matthews et al.*, 2011; *Souza et al.*, 2015]. This makes ROMS an ideal tool to explore the effects of resolution on the mesoscale to submesoscale field and its modulations by ENSO.

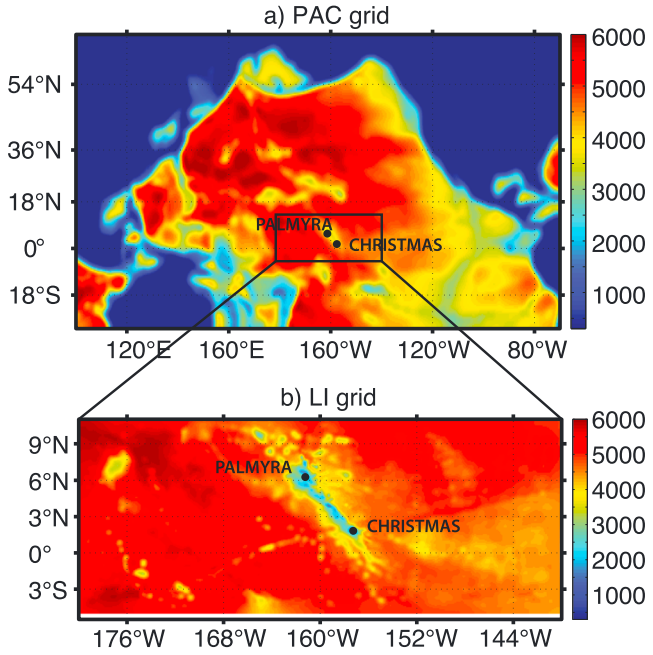

Figure 1. Bathymetry (m) in the isoROMS grids (a) PAC and (b) LI.

Two different ROMS resolutions are employed in this study (Figure 1). The coarse, "parent" grid uses 15 vertical levels and has a variable horizontal resolution ranging from roughly 38 to 50 km; this domain covers the entire Pacific from 30°S to the Bering Strait and is therefore referred to as the PAC grid. The choice of such a large coarse-resolution domain allows any influences from errors in lateral boundary conditions to be neglected, as the northern and eastern boundaries are completely closed and the western boundary encompasses only the Indonesian Throughflow.

From the parent PAC domain, one-way nested downscaling to a uniform 10 km resolution is performed using boundary conditions from the PAC experiment. The downscaling domain covers the region 180°–140°W, 5°S–11°N, and 20 vertical levels are employed to improve vertical resolution; this is referred to hereafter as the Line Islands (LI) domain. LI is an open-ocean configuration, and the boundary conditions were therefore chosen to minimize spurious edge effects. The Chapman condition was used for the free surface [*Chapman*, 1985], a combination of the Flather, radiation, and nudging conditions for momentum [*Flather*, 1976], and a clamped boundary condition was applied to all passive tracers to ensure that they match the lateral boundaries. A sponge layer was applied at the boundaries, where the background viscosity increased from 400 m^2/s to 4000 m^2/s. Along the western boundary, the sponge layer was made twice as wide to ensure that energy created within the domain does not reflect or become trapped at the boundary. In both PAC and LI, the Mellor-Yamada turbulence closure scheme is employed for parameterization of subgrid-scale diffusion/mixing [*Mellor and Yamada*, 1982].

Boundary and initial conditions for temperature, salinity, sea surface height, and ocean currents on the PAC grid were taken from the German contribution to the Estimating the Circulation and Climate of the Ocean (GECCO2) project [*Kohl*, 2014]. Seawater oxygen isotope initial and boundary conditions are derived from the global gridded data set of *LeGrande and Schmidt* [2006], a time-mean data product. The remaining atmospheric fields required to force ROMS (wind speed, heat fluxes, surface humidity, and precipitation) were derived from the Common Ocean-Ice Reference Experiment (CORE2) [*Large and Yeager*, 2008] interannual forcing; all these fields are specified as weekly averages. The CORE2 fields contain only climatological precipitation data prior to 1979; since the topic of interest here is interannual variability, the study period for ROMS has therefore been restricted to 1979–2009.

No spatially and temporally complete set of data exists for precipitation $\delta^{18}O$. As such, a simulation performed with the isotope-enabled version of the National Center for Atmospheric Research (NCAR) Community Atmosphere Model (iCAM5) is used to supply the necessary fields of $H_2^{16}O$ and $H_2^{18}O$ in precipitation.

This simulation used a development version of iCAM5 [*Nusbaumer et al.*, 2014] forced with interannually varying SST from the Hadley Centre Sea Ice and Sea Surface Temperature data set [*Rayner et al.*, 2003]. iCAM5 is derived from the isotopic tracer scheme in an earlier version of CAM (CAM3) [*Noone*, 2006; *Noone and Sturm*, 2010], and the isotopic fractionation follows an approach similar to other isotope-enabled GCMs [see, e.g., *Noone and Sturm*, 2010]. The model agrees favorably with observations from the Global Network for Isotopes in Precipitation, with comparable performance in the tropical Pacific to other models in the SWING2 intercomparison project [cf. *Conroy et al.*, 2014].

We note that the use of CORE precipitation fluxes with iCAM precipitation isotopologue values results in a decoupling between the precipitation amount and the isotopic composition of precipitation, an unavoidable consequence required to maximize agreement with observations. This "hybrid" approach was tested against several alternative configurations: (1) the use of all atmospheric forcing variables taken directly from iCAM5, (2) CORE monthly mean forcing fields with iCAM5 precipitation δ^{18}O, and (3) CORE forcing fields with climatological mean precipitation δ^{18}O, which constituted a set of atmospheric sensitivity experiments. The approach presented here was found to provide the best agreement with observations, as measured by SST, thermocline depth, Oceanic Niño Index, and salinity (not shown). We also note that there are uncertainties associated with internal variability in precipitation δ^{18}O, which is generated independently of SST forcing and which cannot be fully characterized using a single iCAM5 run for precipitation δ^{18}O data; this is expected to lead to an underestimate of the atmospheric forcing influence on seawater δ^{18}O, but a full investigation of these issues is left for future work.

Corrections were applied to the isoROMS surface heat and freshwater fluxes, since the CORE2 atmospheric forcing differs somewhat from the forcing used to create GECCO2 and correcting for this difference is therefore required to keep the ocean and atmosphere in equilibrium. The surface heat flux is modified by a term proportional to the difference in SST between CORE2 and the climatological mean taken from GECCO2 and is a standard technique used to improve ROMS performance [*Haney*, 1971; *Barnier et al.*, 1995]; corrections are on the order of -15 W m^{-2} in the midlatitudes and -45 W m^{-2} in the tropics. The freshwater flux correction is very similar: the difference in salinity between CORE2 and the climatological GECCO2 mean is used to modify the flux term in ROMS, and corrections are on the order of 0.25 m d^{-1} practical salinity unit (psu). Climatological heat and salt flux correction data sets, rather than fully time varying fields, were used to ensure that the mesoscale field represented the true impacts of ENSO variability as closely as possible.

2.2. Atmosphere/Ocean Isotopic Exchange

Seawater oxygen isotopologues $H_2^{16}O$ and $H_2^{18}O$ were added to the ROMS model as passive tracers within the water column. These passive tracers are advected and diffused within ROMS. To close the isotope budget, a surface flux scheme was implemented for isotopologues to control the exchange across the air/sea boundary. The parameterization here follows the *Craig and Gordon* [1965] model, with the inclusion of kinetic effects based on the scheme of *Merlivat and Jouzel* [1979]. This is a typical approach in atmospheric models with isotopic tracer schemes [e.g., *Jouzel et al.*, 1987; *Hoffmann et al.*, 1998; *Noone and Simmonds*, 2002; *Noone and Sturm*, 2010]. In this formulation, the total evaporative flux (E) is considered to have the form

$$\frac{E}{\rho} = \Gamma(q_s - q), \tag{1}$$

where ρ is the air density, q_s the saturation specific humidity at the temperature of the ocean surface, q the specific humidity at the temperature of the top of the atmospheric boundary layer (here assumed equal to the "surface" air temperature specified by the atmospheric forcing file), and Γ is a "profile coefficient" describing turbulent processes within the boundary layer. Specific humidities here are derived from the relative humidity values contained in the CORE2 data set.

An equivalent relationship is written for the evaporative flux of an isotopologue of water ($H_2^{18}O$ or $H_2^{16}O$) [*Merlivat and Jouzel*, 1979]:

$$\frac{E_i}{\rho} = \Gamma(q_{si} - q_i), \tag{2}$$

The specific humidities, q_{si} and q_i, refer to the abundance of the isotopologue, rather than the total atmospheric water content. The isotopic equivalent of the saturation mixing ratio is determined following the

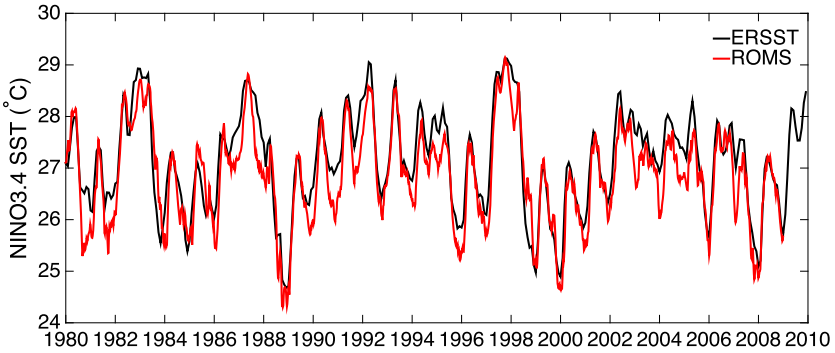

Figure 2. Comparison of SST averaged over the NINO3.4 index region (5°S–5°N, 120–170°W) in the PAC isoROMS simulation (red) as compared with the ERSSTv3b product (black). isoROMS data are taken from the uppermost model level, for a depth range of roughly 0–30 m.

Craig and Gordon [1965] model assuming the existence of a thin laminar layer near the liquid interface at saturation with respect to the surface temperature T_{oce}:

$$q_{si} = q_s \frac{R_{oce}}{\alpha(T_{oce})}, \tag{3}$$

$$q_i = q \frac{R_p}{\alpha(T_{air})}, \tag{4}$$

where R_{oce} and R_p are the respective mole fractions of the isotopologue in seawater and in precipitation. The mixing ratio in precipitation R_p is taken from the isotope-enabled CAM.

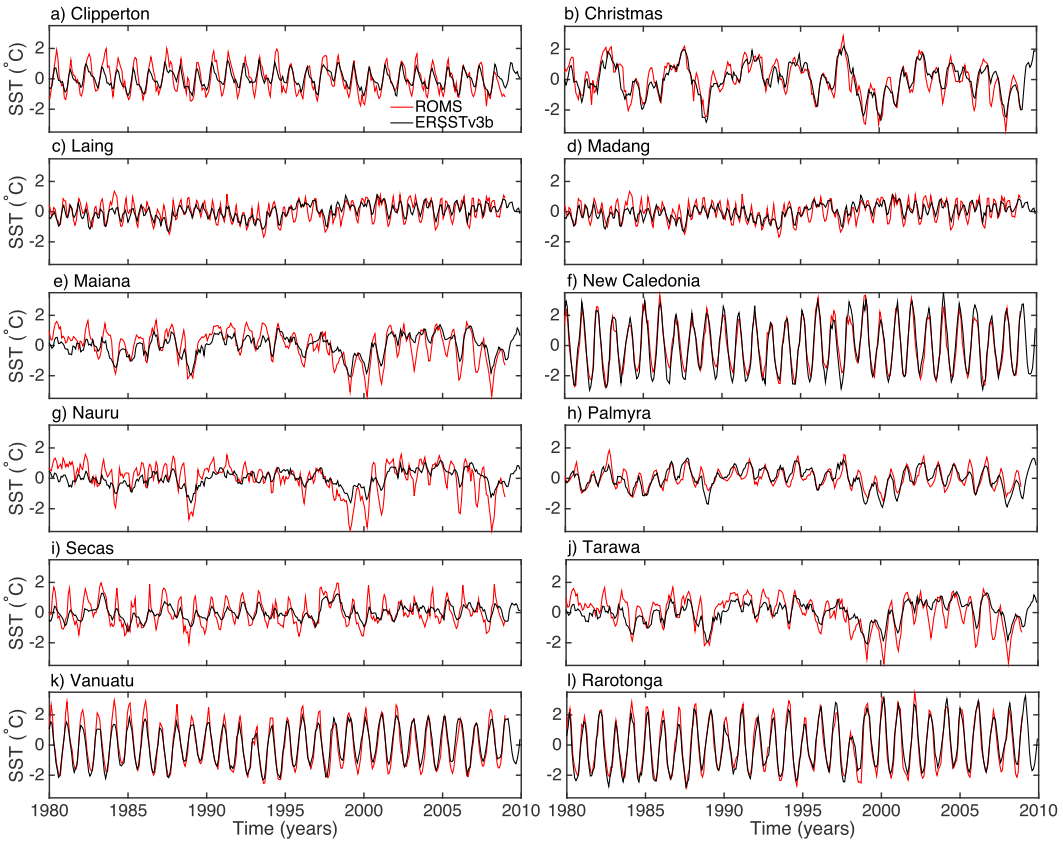

Figure 3. Comparison of isoROMS surface temperature (red) with SST from ERSSTv3b (black). isoROMS data are averaged over a depth range 0–30 m and a latitude/longitude range of ±1° from the location of the proxy site (Table 2).

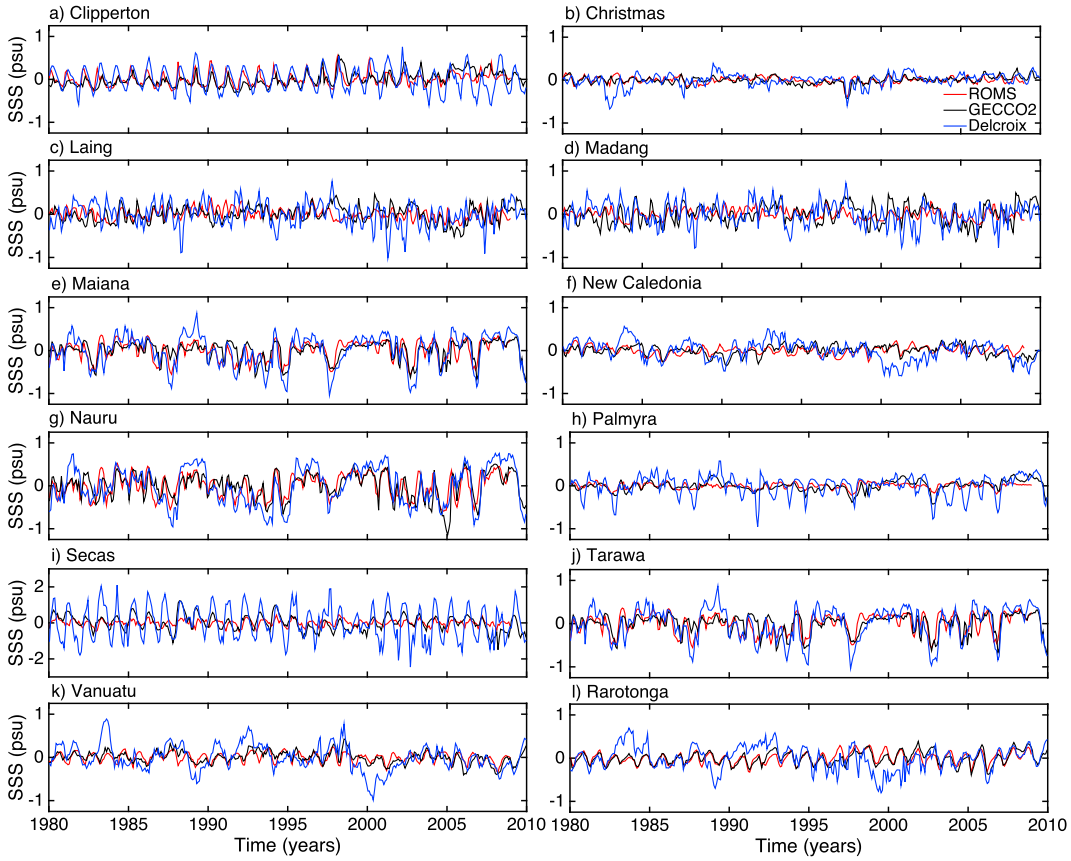

Figure 4. Comparison of isoROMS surface salinity (red) with observational products: GECCO2 (black) and *Delcroix et al.* [2011] (blue). isoROMS data are averaged over a depth range 0–30 m and a latitude/longitude range of ±1° from the location of the proxy site (Table 2).

The total evaporation of the isotopologue is expressed as a fraction of the overall evaporative flux, following the model of *Craig and Gordon* [1965]:

$$\frac{E_i}{E} = (1-k)\frac{(q_{si}-q_i)}{q_s-q}, \tag{5}$$

where the kinetic fractionation factor k is computed following *Merlivat and Jouzel* [1979].

Finally, the net flux of isotopologues into the upper layer of the ocean is computed, as the difference between precipitative and evaporative fluxes

$$F = PR_p - \left[(1-k)\frac{(q_{si}-q_i)}{(q_s-q)}\right]E, \tag{6}$$

where the total evaporation E is determined by the difference between the prescribed precipitative and net freshwater fluxes taken from CORE2 and GECCO2, respectively.

2.3. Model Validation

The performance of the model is tested by comparing the PAC simulation to observational products. Figure 2 shows the sea surface temperature (SST) computed over the NINO3.4 index region (5°S–5°N, 120–170°W) from the Extended Reconstructed SST product version 3 (ERSSTv3b) [*Smith et al.*, 2008], compared with the same quantity computed from the uppermost model level in the PAC simulation. Performance is quite good overall; the two are correlated at $R^2 = 0.91$, and the magnitudes of El Niño events are extremely well simulated by isoROMS. There is some tendency for isoROMS to exaggerate the magnitudes of cold anomalies, which could potentially relate to the comparison of observational SST with ROMS bulk temperature (averaging over the uppermost model level generally corresponds to a 0–30 m mean in the central equatorial Pacific).

Table 1. R^2 Values for the PAC Simulation, Compared With Observations of SST (ERSSTv3b), SSS (GECCO2), and Coral $\delta^{18}O$ (Modern Records in Table 2)[a]

Site	SST	SSS	$\delta^{18}O$	RMS_{R-G2}	RMS_{G2-D}
[e]Clipperton	0.69	0.32	0.24	0.14	0.32
[c]Kiritimati	0.77	0.43	0.49	0.10	0.16
[w]Laing	0.58	0.17	0.065	0.17	0.41
[c]Maiana	0.61	0.44	0.52	0.19	0.26
[s]New Caledonia	0.93	0.15	0.35	0.12	0.25
[c]Nauru	0.49	0.44	0.57	0.24	0.31
[c]Palmyra	0.65	0.36	0.52	0.10	0.26
[e]Secas	0.55	0.16	0.0016	0.47	1.62
[c]Tarawa	0.61	0.44	0.31	0.19	0.26
[s]Vanuatu	0.89	0.41	0.52	0.11	0.26
[s]Rarotonga	0.93	0.65	0.67	0.11	0.27

[a]ROMS temperature and salinity values have been depth averaged over 0–30 m and horizontally averaged over a $2 \times 2°$ area surrounding the location of the coral site; ROMS $\delta^{18}O$ values are also depth averaged over 0–30 m but are taken from the PAC grid point at the minimum Euclidean distance from the proxy location. Superscript letters refer to the region in which the site is located: "e" (eastern equatorial Pacific), "c" (central equatorial Pacific), "w" (western equatorial Pacific), or "s" (southwestern Pacific). The rightmost columns provide salinity RMS errors for isoROMS versus the GECCO2 product (RMS_{R-G2}) and for the GECCO2 versus *Delcroix et al.* [2011] products (RMS_{G2-D}), respectively.

Further testing of model accuracy is provided in Figures 3 and 4, which show isoROMS surface temperature and salinity as compared with observations for 10 different locations where coral $\delta^{18}O$ records have been collected; these are the same sites used in *Stevenson et al.* [2013]. SST data are taken from the ERSSTv3b product and salinity from the GECCO2 state estimate, and the isoROMS data are averaged over a 1° region to match the grid resolution of the data products. The model does well at simulating temperature at all locations, with R^2 values ranging from 0.55 to 0.93 (Table 1). There is a slight overestimation of the annual cycle amplitude at some locations, but at the Line Islands the magnitude of variability appears qualitatively consistent with observations. This gives confidence that the downscaling simulations in sections 3 and 4 for Palmyra and Christmas will yield reliable results.

The simulation of salinity is considerably more difficult than that of temperature owing to the need to correctly represent the global hydrological cycle [*Stephens et al.*, 2010; *Durack et al.*, 2012]. This difficulty is reflected in the performance of isoROMS: Table 1 shows that the R^2 values are generally lower for salinity, ranging from 0.15 to 0.65. The more limited success of the salinity simulation is likely mirrored in the $\delta^{18}O$ simulations, which also depend on the simulated freshwater budget. Figure 4 shows grid point salinity time series from ROMS, GECCO2, and the *Delcroix et al.* [2011] salinity product: the magnitude of El Niño-/La Niña-related salinity excursions are well captured in some locations (most notably Tarawa, Maiana, Nauru, and Christmas), but performance is relatively poor in others (i.e., Laing, Secas, and New Caledonia). Performance seems worst at sites dominated by influences of the Intertropical Convergence Zone and South Pacific Convergence Zone, potentially reflecting issues with precipitative flux representation in CORE. However, even at locations where isoROMS does not agree well with GECCO2, the inclusion of the *Delcroix et al.* [2011] gridded product in Figure 4 serves as demonstration that data-based estimates of salinity contain substantial uncertainties themselves. The magnitude of salinity variations is much larger in the *Delcroix et al.* [2011] product than in GECCO2 at many locations, particularly those dominated by an annual cycle (i.e., Clipperton, Secas, and Rarotonga). The root-mean-squared errors between isoROMS and GECCO2 are less than those between GECCO2 and the *Delcroix et al.* [2011] product at all locations; thus, isoROMS can be considered to be representing surface salinity to within the limits of uncertainty.

Figure 5 shows isoROMS simulation of coral $\delta^{18}O$, taken from the grid point with the minimum Euclidean distance from the location of the coral collection site (see also Table 2). The uppermost model vertical level is used in all cases, as an investigation of the collection depths of each coral (Table 2) showed that all corals were growing in water shallower than 18 m at the time of collection. Coral $\delta^{18}O$ is calculated as

$$\delta^{18}O_{coral} = \delta^{18}O_{seawater} - 0.21T, \quad (7)$$

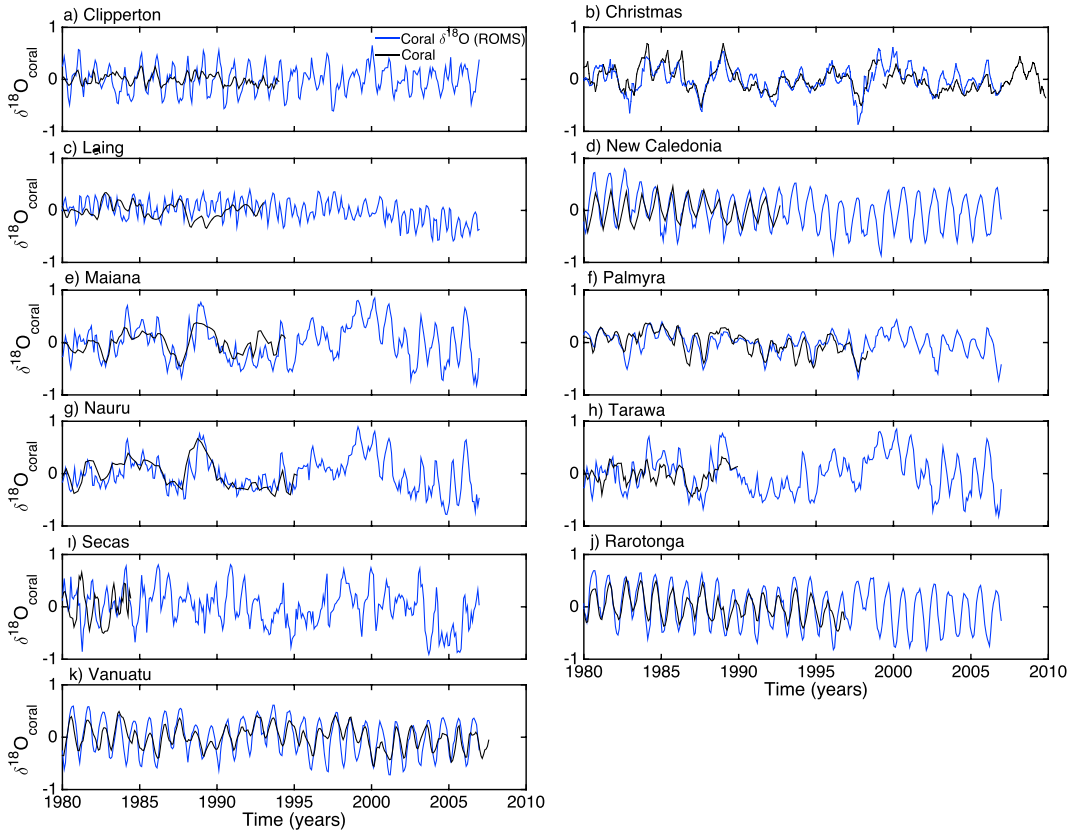

Figure 5. Comparison of ROMS-derived coral δ^{18}O (blue) with modern coral δ^{18}O time series (black). ROMS data are averaged over a depth range 0–30 m, and the horizontal grid point closest to the location of the proxy site is used (Table 2).

where the proportionality constant of −0.21‰/°C is a representative value for the temperature dependence observed in tropical corals (typically −0.18 to −0.22) [*Gagan et al.*, 2012] and $\delta^{18}O_{seawater}$ is computed from the modeled water isotopologues using Vienna Standard Mean Ocean Water as the reference standard.

IsoROMS results are compared with coral δ^{18}O records taken from the World Data Center for Paleoclimatology (data references in Table 2); at all locations, isoROMS is able to capture ENSO-related variability in the δ^{18}O records, although at some sites (i.e., Clipperton) the magnitude of the seasonal δ^{18}O cycle is overestimated.

Table 2. Collection Depths for Modern Corals Used to Construct δ^{18}O Time Series, as Retrieved From the World Data Center for Paleoclimatology[a]

Site	Reference	Depth	Latitude	Longitude
Clipperton	*Linsley et al.* [1994]	8–13 m (3 cores)	10.3°N	250.78°E
Kiritimati	P. R. Grothe et al. (personal communication, 2015)	≈10 m	1.87°N	202.6°E
Laing	*Tudhope et al.* [2001]	3 m	4.15°S	144.88°E
Maiana	*Urban et al.* [2000]	6 m	1°N	173.0°E
New Caledonia	*Quinn et al.* [1998]	3 m	22.48°S	166.45°E
Nauru	*Guilderson and Schrag* [1999]	14 m	0.5°S	166.0°E
Palmyra	*Cobb et al.* [2003]	9.1 m	5.87°N	197.87°E
Secas	*Linsley et al.* [1994]	3 m	7.98°N	277.95°E
Tarawa	*Cole et al.* [1993]	3 m	1°N	173.0°E
Vanuatu	*Gorman et al.* [2012]	8 m	15.94°S	166.04°E
Rarotonga	*Linsley et al.* [2006]	18 m	21.23°S	200.18°E

[a]Sites are listed alphabetically here and in Table 1.

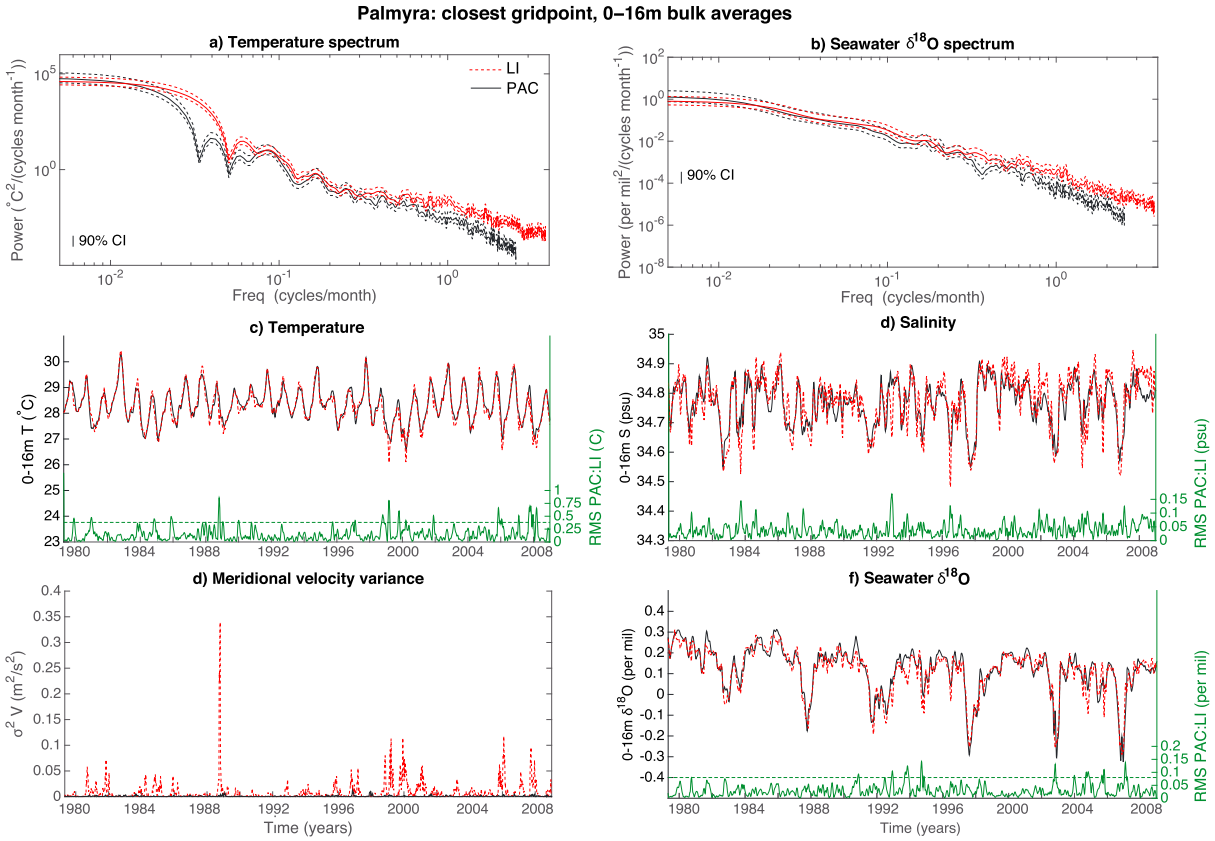

Figure 6. Spectra of (a) temperature and (b) seawater δ^{18}O at Palmyra, for the PAC (black) and LI (red) isoROMS simulations. Spectra are computed using Welch's averaged, modified periodogram spectral estimation method with a 300-point Hann window, overlapping by 30%. (c) 30-day running mean temperature at Palmyra for PAC (black) and LI (red), with the RMS error between the PAC and LI temperatures plotted in green on the right-hand axis. (d) Same as Figure 6c but for salinity. (e) Variance of meridional velocity, computed over a 30 day running window, in PAC (black) and LI (red). (f) Same as Figure 6c) but for seawater δ^{18}O. All ROMS data are taken from the uppermost model level and the grid point closest to Palmyra. Dashed horizontal green lines in Figures 6c and 6f indicate the detection limit for a PAC/LI offset in a coral δ^{18}O record given observational uncertainty (0.08‰ or 0.38°C).

In general, the model appears to perform better in temperature-dominated settings (i.e., the central Pacific sites like Maiana, Nauru, Tarawa, and Christmas), although temperature errors also come into play for sites dominated by the annual cycle. Generally, R^2 values for $\delta^{18}O_{coral}$ range from 0.25 to 0.6 (Table 1) and lie between the R^2 values for temperature and salinity at all locations.

3. Mesoscale Influences: Palmyra

The isoROMS experimental configuration allows a direct assessment of the contribution of small-scale processes to conditions near Line Islands reefs, by comparison of results from the PAC and LI simulations. Figure 6 shows temperature, salinity, and seawater δ^{18}O time series from the grid point located closest to Palmyra Atoll (5.9°N, 162.1°W) in both isoROMS experiments. Substantial (0.5°C or larger) offsets in 0–30 m temperature between the Pacific and Line Islands experiments are present during certain time periods (Figure 6c). The offsets are largest during cold periods, and the boreal winter seasons 1983–1984, 1999–2000, and 2007–2008 are particularly good examples. At these times the PAC/LI temperature differences are 0.5–0.8°C, as measured by the 30 day running root-mean-squared error (RMS) between PAC and LI. For "standard" assumptions regarding inorganic aragonite precipitation [*Gagan et al.*, 2012], these temperature differences should result in easily detectable coral δ^{18}O offsets of over 0.1‰. During warm periods (i.e., early 1984, 1988, and 2005), there is a slight tendency for enhanced LI warming, although this effect is not as easily detectable; examination of the zonal current profiles (not pictured) suggests that this may relate to enhanced transport in the North Equatorial Countercurrent (NECC) at higher resolution, possibly due to interaction of flow with topography at Palmyra [*Hamann et al.*, 2004].

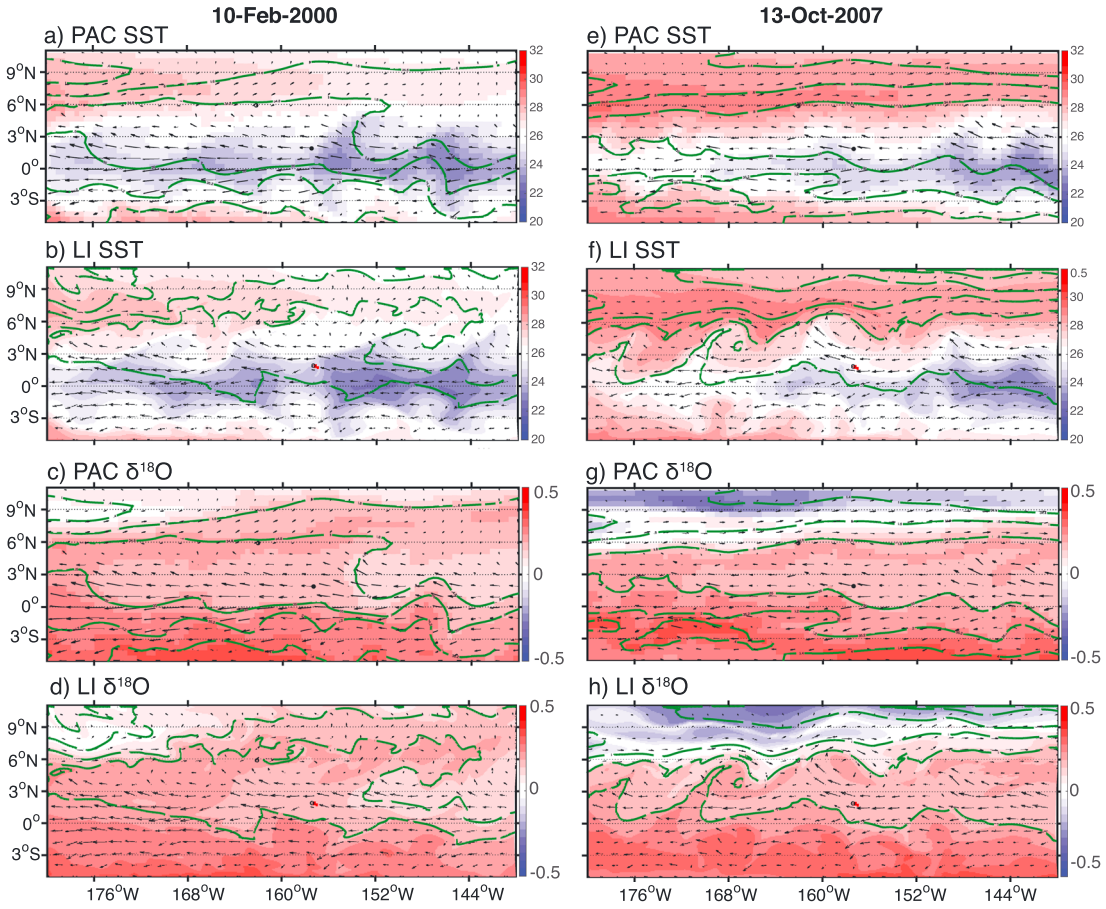

Figure 7. Snapshots of SST and seawater $\delta^{18}O$ in the Line Islands region, demonstrating the difference between tropical instability wave behavior in PAC and LI. Colors indicate (a, b, e, and f) temperature or (c, d, g, and h) seawater $\delta^{18}O$; arrows indicate surface (0–16 m) currents. Black filled circles indicate the locations of Palmyra and Christmas Islands. Contours indicate 0–30 m salinity, which is contoured from 34.2 to 35.4 by 0.2 psu.

Salinity and seawater $\delta^{18}O$ offsets are shown in Figures 6d and 6f: changes to seawater $\delta^{18}O$ as a function of resolution do exist but are smaller than the offsets in temperature and generally range from 0.05 to 0.1‰. These changes would therefore be difficult to detect given observational uncertainty (0.05–0.08‰) [*McGregor et al.*, 2011; *DeLong et al.*, 2013], although this might be possible at some times. The salinity changes from PAC to LI are on the order of 0.1–0.2 psu (Figure 6d), and periods of low-salinity excursions in LI

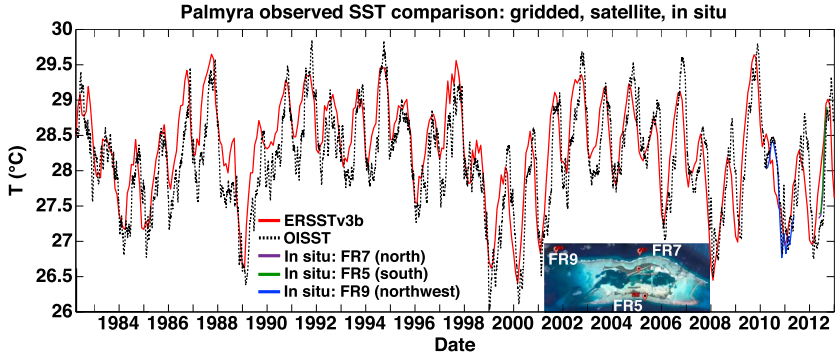

Figure 8. Comparison of the ERSSTv3b gridded product (red) with the AVHRR OISST satellite product (black dashed), as well as in situ temperature data collected by the NOAA Coral Reef Ecosystem Division (CRED) at Palmyra. The locations of the in situ measurements are shown on the inset map, and CRED data are plotted as the purple (FR7, north shore), green (FR5, south shore), and blue (FR9, northwest corner) lines.

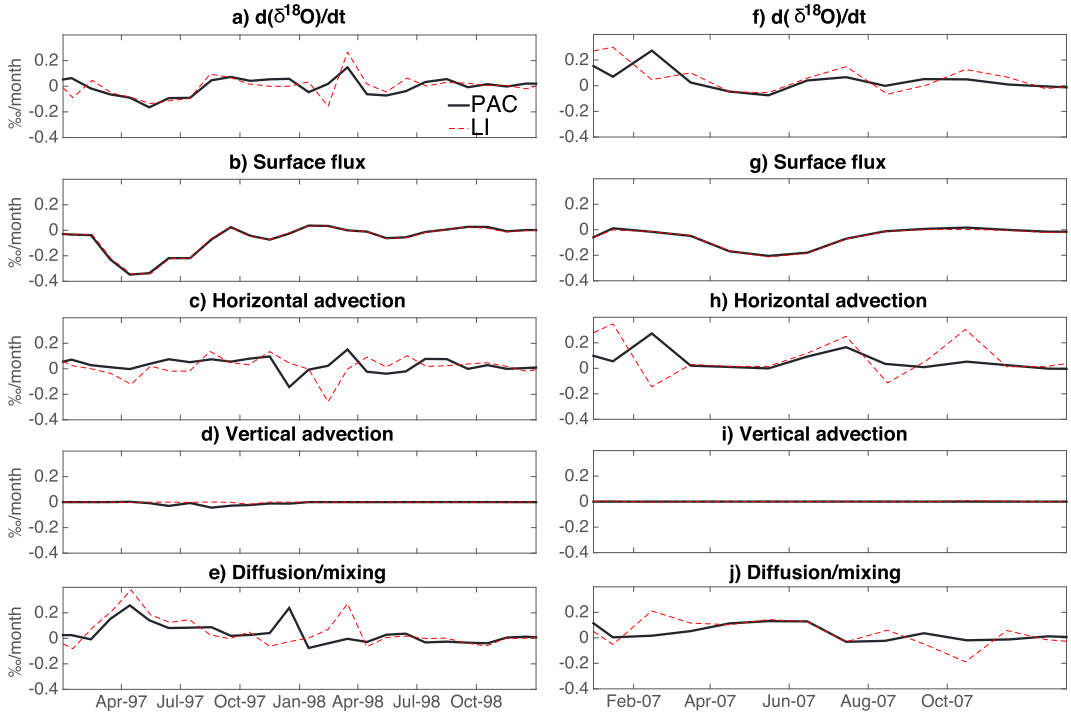

Figure 9. Terms in the budget of seawater δ^{18}O at Palmyra. Values shown correspond to the grid point closest to Palmyra in the PAC (black) and LI (red dashed) isoROMS simulations. (a–e) Budget time series for January 1997 to January 1999. (f–j) Same as Figures 9a–9e but for January–December 2007.

(i.e., late 1983 and winter 1992–1993) are not always accompanied by increases in seawater δ^{18}O (Figure 6f), as one would expect based on linear pseudoproxy assumptions [*LeGrande and Schmidt*, 2006; *Thompson et al.*, 2011]. The mechanism for PAC/LI salinity differences appears to be the passage of meridional fronts past Palmyra, which carry larger gradients in salinity than δ^{18}O (not pictured). These effects have implications for salinity reconstructions from seawater δ^{18}O and will be investigated further in a follow-up paper.

Cold temperature anomalies in LI appear to be generated by tropical instability waves (TIWs). TIW passage generates strong anomalies in the local flow field, and the running variance of meridional velocity is therefore taken as a rough indicator of TIW activity. Peaks in this quantity are strongly related to the RMS difference in PAC/LI temperature, with maxima in variance occurring during cold periods in LI. Figures 6a and 6b show the spectra of temperature and seawater δ^{18}O computed at the location of Palmyra: spectral slopes are shallower at high frequencies (less than 30 day periods) in the LI simulation, consistent with the expected reduction in energy dissipation [*Marchesiello et al.*, 2011]. Additionally, there is a clear enhancement in the power near one cycle per month in LI, which coincides with the frequency range generally associated with TIWs (17–40 days) [*Lyman et al.*, 2007]. The power at interannual frequencies also appears to be enhanced, which is likely due to the fact that TIWs occur more frequently during the cold phase of ENSO [*Yu and Liu*, 2003; *An and Jin*, 2004; *An*, 2008].

Snapshots of the temperature, salinity, and seawater δ^{18}O surface fields are shown in Figure 7 for February 2000 and January 2007, two periods where strong PAC/LI temperature offsets are observed. At both times, SST patterns resembling the "canonical" TIW are clearly visible (Figures 7a, 7e, 7b, and 7f), with cold equatorial SST and cusplike filaments of cold water associated with anticyclonic tropical instability vortices extending to the north and south. Comparing Figures 7a/7b and 7e/7f, it is apparent that the vortex structures are much more highly developed at 10 km resolution, while in PAC the meridional currents and frontal gradients are nearly absent. This is consistent with the results of *Marchesiello et al.* [2011], who found that convergence of the equatorial kinetic energy spectrum occurred near 10 km resolution and concluded that this is a minimum required resolution to properly capture mesoscale variations associated with TIWs.

Mesoscale temperature variations at Palmyra are next compared between the 1° gridded ERSSTv3b product and the satellite-derived 0.25° NOAA Optimum Interpolated SST data set [*Reynolds et al.*, 2002], as well as in

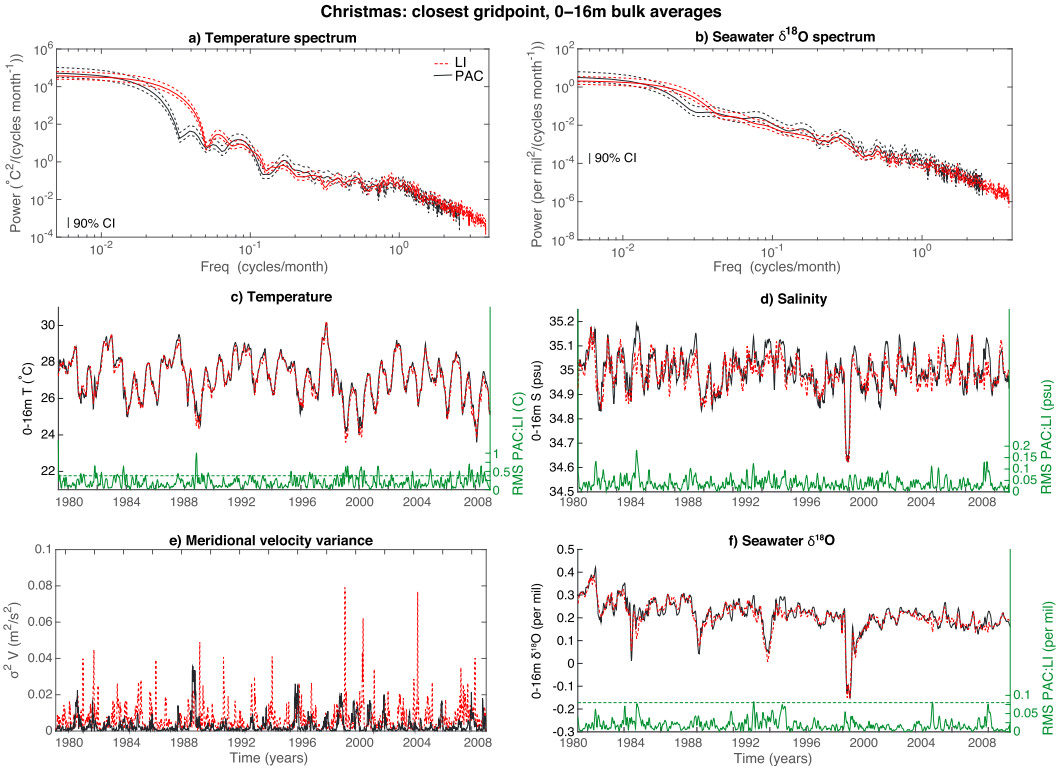

Figure 10. Same as Figure 6 but for grid point closest to Christmas. In the LI run, the grid point nearest Northeast Point is used (see text for details).

situ temperature data collected by the NOAA Coral Reef Ecosystem Division during regular surveying expeditions to Palmyra (J. Gove, personal communication; Figure 8). The OISST time series shows a clear tendency for cold excursions during boreal winter and strong La Niña events (i.e., the 1998–1999 and 2010–2011 winter seasons), consistent with the behavior of isoROMS.

To examine the processes altering the concentration of seawater δ^{18}O at Palmyra, the δ^{18}O budgets are computed at the grid point closest to Palmyra in the PAC and LI simulations. The budget of δ^{18}O is derived from the budgets of the $H_2^{16}O$ and $H_2^{18}O$ isotopologues, each of which have the form

$$\frac{\partial O}{\partial t} + \vec{v} \cdot \nabla O = \Phi + D, \tag{8}$$

where $\vec{v}$ is the three-dimensional velocity, O refers either to $H_2^{16}O$ or $H_2^{18}O$, and the term D includes horizontal dissipation and vertical diffusion. The forcing term Φ is the net addition of isotopologue mass to the ocean via precipitation, after subtraction of the upward evaporative flux (see section 2.2).

Applying the quotient rule (see appendix for derivation), the budget equation for the isotopic ratio R is

$$\frac{\partial R}{\partial t} = \underbrace{\frac{1}{H_2^{16}O}\left(\Phi_{H_2^{18}O} - R\Phi_{H_2^{16}O}\right)}_{\text{Surface Flux}} + \underbrace{\frac{1}{H_2^{16}O}\left(-\vec{v} \cdot \nabla H_2^{18}O + R\vec{v} \cdot \nabla H_2^{16}O\right)}_{\text{Advection}} + \underbrace{D_R}_{\text{Diffusion/Mixing}} \tag{9}$$

where $R = H_2^{16}O/H_2^{18}O$ and a multiplicative factor is used to convert to δ^{18}O units (see appendix).

The time series of each term in (9) is shown in Figure 9 for Palmyra. Here the focus is on two time slices within the simulation period: the 1997–1998 El Niño event and the La Niña year 2007. The surface flux terms are identical between PAC and LI (Figures 9b and 9g), since the same atmospheric forcing is used in both cases. Differences appear in the advective and diffusive terms (Figures 9c–9e and 9h–9j), which experience larger magnitudes in LI relative to PAC and are associated with changes in $d(\delta^{18}O)/dt$. This is particularly apparent during the winter of 2007, when anomalies in horizontal advection track $d(\delta^{18}O)/dt$ (Figures 9a and 9c),

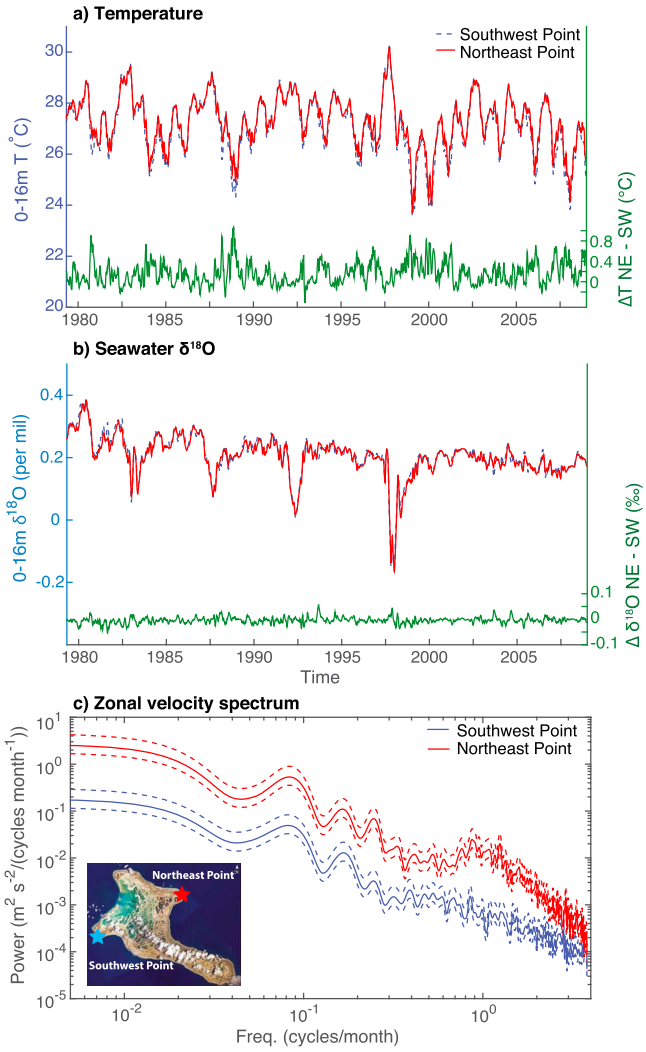

Figure 11. (a) 0–30 m time series of temperature from the LI ROMS run, for grid points closest to two locations on Christmas Island (Southwest Point and Northeast Point, shown in the inset map in Figure 11c). Values plotted in green are the difference between 0 and 30 m temperatures at Northeast Point versus Southwest Point. (b) 0–30 m time series of seawater $\delta^{18}O$, for the same locations as Figure 11a. Difference in $\delta^{18}O$ between Northeast Point and Southwest Point is plotted in green. (c) Spectra of 0–30 m zonal velocity in the LI ROMS run for the same locations in Figure 11b. Dashed lines in Figure 11c indicate the 90% confidence intervals on spectral power. Spectra are computed using Welch's averaged, modified periodogram spectral estimation method with a 300-point Hann window, overlapping by 30%.

albeit with some compensation by vertical mixing/diffusion. This is consistent with the enhanced TIW activity documented above, and one occasional source for the strengthened horizontal advection is the enhanced TIW activity during boreal winters.

4. Mesoscale Influences: Christmas

We next investigate the dynamics influencing conditions at Kiritimati (Christmas) Island (1.9°N, 157.4°W). At 388 km^2, Christmas is large enough that the land mass is resolved in LI; this requires additional care when selecting appropriate grid points to compare with PAC. As a first illustration, Figure 10 shows temperature, salinity, and seawater $\delta^{18}O$ time series and spectra for the grid point with the minimal Euclidean distance to Christmas, equivalent to the quantities shown in Figure 6. As was the case at Palmyra, the largest differences in PAC versus LI temperature are associated with enhanced variance in LI meridional velocity (Figures 10c and 10e), suggesting a role for eddy activity. PAC:LI temperature changes are smaller than at Palmyra, remaining below 0.5°C at most times but with some larger excursions at times of high TIW activity (see the RMS

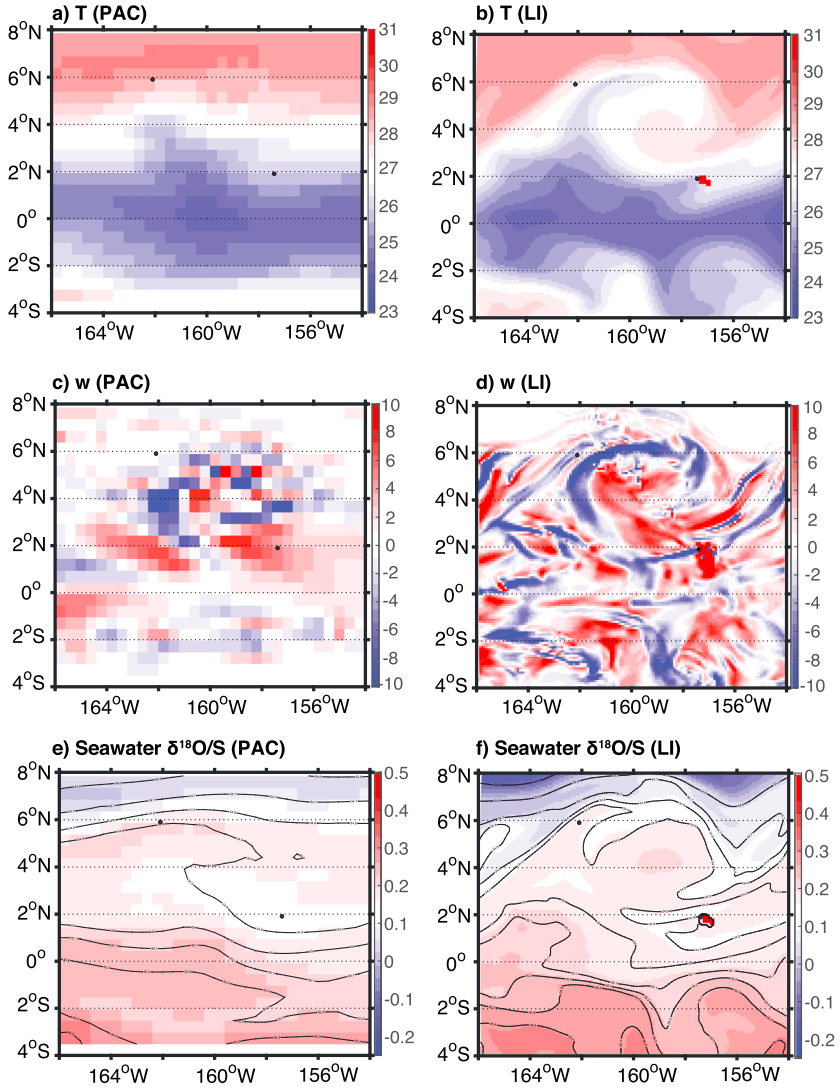

Figure 12. Passage of an October 2007 tropical instability wave event by Palmyra and Christmas in (a, c, and e) PAC and (b, d, and f) LI. Dates plotted are the PAC/LI times lying closest to 20 October 2007. Temperature (°C) in uppermost model level (Figures 12a and 12b), for vertical *w* velocity (m/d) (Figures 12c and 12d), and for seawater δ^{18}O (per mil; colors) and salinity (psu; contours) (Figures 12e and 12f). Salinity contour interval is 0.1 psu, maximum/minimum values 34.5–35.4. Black filled circles indicate the locations of Palmyra and Christmas Islands.

curves in Figure 10c). Offsets are visible in salinity and seawater δ^{18}O, but these effects are relatively modest and are not expected to be easily detectable given a coral δ^{18}O record.

Taken alone, Figure 10 might indicate that no mesoscale influences significantly affect temperature or seawater δ^{18}O at Christmas. But a more careful investigation reveals that the story is more complicated: in Figure 11, time series from the LI grid points closest to two different, known coring locations for coral δ^{18}O at Christmas are shown. These are Northeast Point (1.9901°N, 157.3141°W) [*Woodroffe et al.*, 2003; *Woodroffe and Gagan*, 2000] and Southwest Point (1.8737°N, 157.5615°W) [*Evans et al.*, 1998]. Corals have also been collected from Cecile Peninsula slightly to the east of the Southwest Point location [*McGregor et al.*, 2011] and from the leeward side of the island south of the entrance to the lagoon [*Nurhati et al.*, 2009]; these locations are considered equivalent to Southwest Point for these purposes, as even the 10 km LI resolution may not be sufficient to distinguish between them.

Figures 11a and 11b show time series of LI temperature and seawater δ^{18}O, respectively, from Northeast and Southwest Points. Time series from the two sites track closely in both variables, and temperature in particular is indistinguishable during neutral to warm periods. However, during cold periods the differences

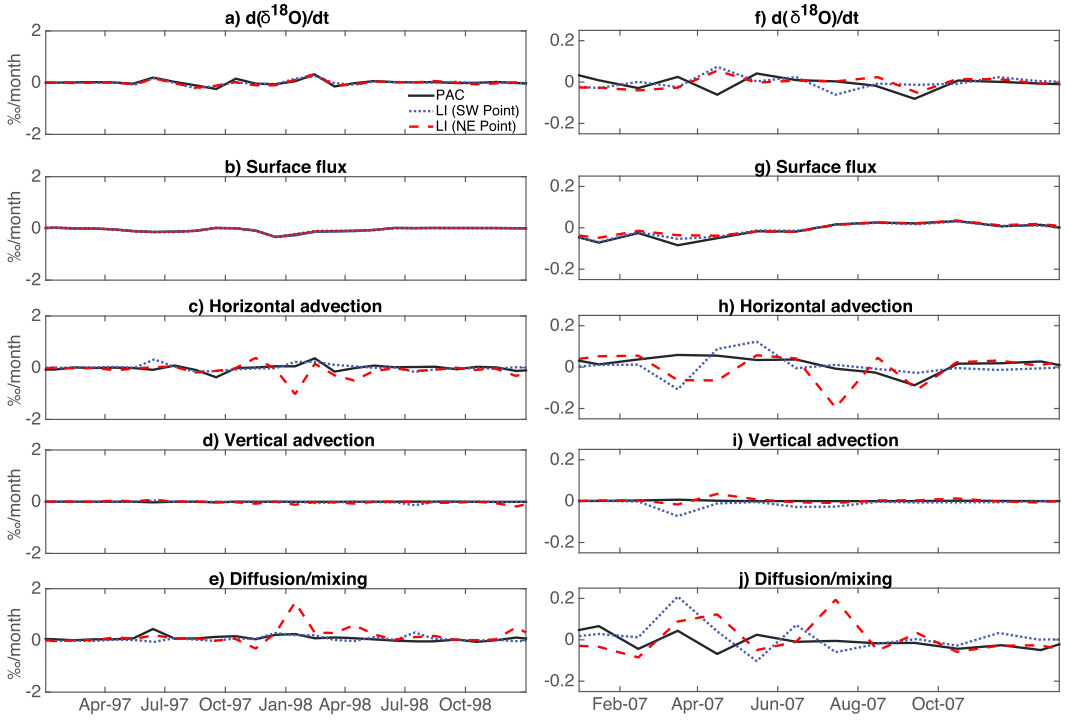

Figure 13. Budget for seawater δ^{18}O at Christmas. Values shown correspond to the grid point closest to the island in the PAC and LI ROMS simulations. Values for PAC are plotted in black, while the LI time series nearest Northeast Point and Southwest Point appear in red and blue, respectively. (a–e) Budget time series for January 1997 to January 1999. (f–j) Same as Figures 13a–13e but for January–December 2007. Note the differences in vertical axis range between Figures 13a–13e and 13f–13j.

in temperature can become substantial—offsets of nearly 1°C (−0.2‰) are seen several times over the simulation period (cf. RMS curve in Figure 11a). During these times, Northeast Point is systematically warmer than Southwest Point, suggesting a role for flow-topography interaction in generating the temperature differences.

The incidence of TIW fronts at Christmas appears to be responsible for generating much of the Northeast Point-Southwest Point temperature differences. As for Palmyra, the largest RMS differences occur during cold periods and coincide as well with time periods of large meridional velocity variance (see Figure 10e). A representative example of the passage of a TIW event past Christmas is shown in Figure 12, focusing on the Line Islands in temperature, vertical velocity, and seawater δ^{18}O. At 50 km resolution, the fronts are not well developed in any variable, consistent with *Marchesiello et al.* [2011]. However, as seen in section 3 the LI grid is able to resolve much more of the TIW's structure, including the strong vertical velocity anomalies following the edge of the front. But the most striking feature of Figure 12 is the clear filamentary structure stretching west from Christmas, which is associated with cooler temperatures at Southwest Point. This is a qualitative indication that TIW wake effects may be influential in this case. Providing further support for the TIW wake hypothesis, the spectra of zonal velocity at the two locations are shown in Figure 11c; the TIW-related spectral peak at ≈30 day periods is enhanced at Northeast Point relative to Southwest Point.

We have also investigated the possibility of cross-island temperature changes generated by the Equatorial Undercurrent, as Christmas is near the climatological latitudinal range of the EUC, and EUC transport tends to strengthen during La Niña events [*McPhaden and Hayes*, 1990]. However, EUC activity does not appear to be the primary driver of these temperature gradients; during periods of strong Northeast Point/Southwest Point temperature offsets, the EUC tends to be located within 1° of the equator and shows little association with upwelling at the surface near Southwest Point (not pictured).

The budget of seawater δ^{18}O at the closest PAC grid point to Christmas is shown in Figure 13, along with the LI budgets at Northeast and Southwest Points. As at Palmyra, the time domain has been restricted to the 1997–1998 and 2007 periods. Once again, resolution does not significantly influence the surface fluxes or the isotope ratio of the fluxes (Figures 13b and 13g). However, in late 2007 there are some high-frequency

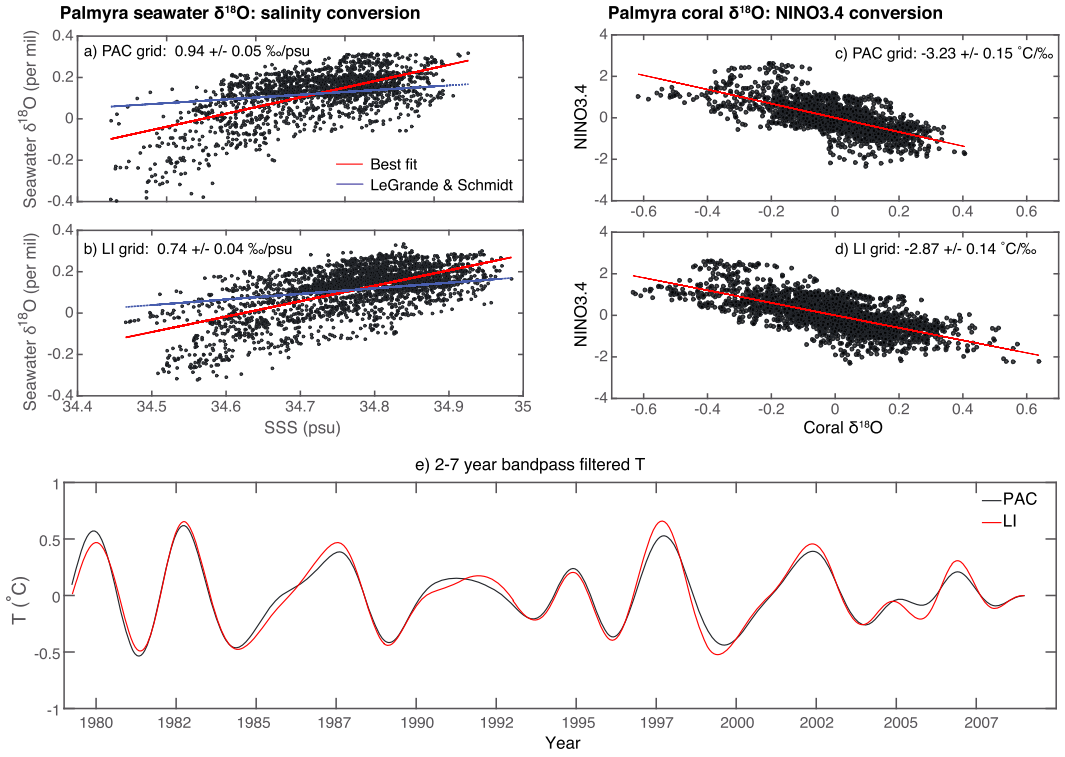

Figure 14. (a and b) Relation between surface salinity and seawater δ^{18}O at Palmyra, in PAC and LI, respectively. Red line indicates the least squares regression slope quoted in the legend for each panel, and the blue line is the 0.27°/psu slope derived from the *LeGrande and Schmidt* [2006] data set. (c and d) Relation between 0 and 30 m coral δ^{18}O anomaly and NINO3.4 SSTA at Palmyra, in PAC and LI. (e) 2–7 year band-pass-filtered time series of Palmyra surface temperature in PAC (black) and LI (red).

excursions in the total time rate of change in LI which are not apparent in PAC (Figure 13f), along with an overall increase in the magnitude of horizontal advective anomalies in LI (Figure 13h). The increases in both advective and diffusive anomalies in LI versus PAC are much larger than the changes in $\partial\delta^{18}\mathrm{O}/\partial t$ (Figures 13f, 13h, and 13j), indicating that signals transmitted horizontally are more efficiently mixed with the subsurface as a result of higher resolution. This effect is much stronger at Christmas than Palmyra, and the advective/diffusive signals differ dramatically between Northeast and Southwest Points due to the differences in the mesoscale field at these locations. During the 1997–1998 El Niño, PAC/LI changes in $\mathrm{d}(\delta^{18}\mathrm{O})/\mathrm{d}t$ are less pronounced, despite large changes in the advective budget terms (Figures 13c and 13e); this suggests an active role for vertical mixing in dispersing horizontally advected signals.

5. Implications for ENSO Reconstruction

A goal of this study is to provide a physically based assessment of the controls on seawater δ^{18}O and consequently improve our ability to infer climate variability from coral δ^{18}O. Previous work [*Stevenson et al.*, 2013] has demonstrated that using linear regression of δ^{18}O on coarse-resolution gridded SST and sea surface salinity (SSS) products leads to prohibitively large errors on δ^{18}O variance. The results of this study indicate that mesoscale to submesoscale variability is a significant source of these errors.

The difficulty with linear "pseudoproxies" is illustrated for Palmyra in Figure 14: Figures 14a and 14b show the relation of isoROMS salinity and seawater δ^{18}O, in both PAC and LI. There is substantial uncertainty in both relationships, and R^2 values are roughly 0.4 in both cases. For PAC, the pseudoproxy slope is 0.94‰/psu, and in LI the slope is reduced by roughly 20% to 0.74‰/psu. Both are substantially steeper than the 0.27‰/psu value predicted by the basin-wide relation of *LeGrande and Schmidt* [2006] and the slightly higher slopes measured by *Conroy et al.* [2014] (0.3 to 0.4‰/psu for the upper water column). Interestingly, the same pseudoproxy slopes computed for Christmas are 0.46‰/psu in PAC and 0.49 in LI (not pictured), closer to the canonical

observational values and indicating a potential for large spatial variability in the salinity:seawater $\delta^{18}O$ slope across the Line Islands. Comparing Figures 14a and 14b then shows that the scatter in seawater $\delta^{18}O$ is larger in LI, particularly for the negative $\delta^{18}O$ portion of the phase space: as alluded to above, small-scale (and short-timescale) processes are most likely responsible for altering the SSS:$\delta^{18}O$ relationship in subtle ways not well captured by a simple linear regression.

Given the issues with linear seawater $\delta^{18}O$:salinity conversions, one potential alternative is to relate coral $\delta^{18}O$ directly to the climate variable of interest. Figures 14c and 14d show the isoROMS NINO3.4 SST anomaly regressed on coral $\delta^{18}O$ in PAC and LI. The R^2 values here are larger than the seawater $\delta^{18}O$:salinity relations, owing to the strong temperature control on coral $\delta^{18}O$ at the Line Islands, but once again, there is a fairly large (1 to 2°C) range of possible SST anomalies associated with a given $\delta^{18}O$ value. A comparison of Figures 14c and 14d then also shows that increased model resolution results in a reduction of the linear regression slope: the "tails" of the $\delta^{18}O$ distribution widen, as more extreme El Niño and La Niña events create large temperature and/or seawater $\delta^{18}O$ excursions driven by mesoscale processes. The reduction in NINO3.4:coral $\delta^{18}O$ slope is significant at the 90% level and is sufficient to generate a 15% difference in ENSO variance.

Figure 14 helps to reinforce the notion that even when reconstructing large, basin-scale signals, simple linear regressions are not the optimal method for creating coral:climate transfer functions; the true relationship is nonlinear, and nonlinear controls on $\delta^{18}O$ will be presented in a follow-up paper. Based on the present work, it is clear that any conversion method which hopes to capture the true dynamical relationships between coral $\delta^{18}O$ and ENSO should ideally account for potential mesoscale influences on the reef. If local processes are smaller than the island of interest, these effects might be mitigated by averaging multiple $\delta^{18}O$ records, as is becoming more standard in the field [*Cobb et al.*, 2013; *DeLong et al.*, 2013; *Dassie et al.*, 2014]. However, the TIW frontal effects documented here will not be eliminated by such methods, since they are significantly larger than the atolls themselves. This was tested using isoROMS grid point data for both temperature and $\delta^{18}O$ (not shown). Obtaining further in situ data to verify the isoROMS results will also be critical, and efforts to increase monitoring at coral sites are highly recommended. The degree to which coral composites can "average out" mesoscale influences is also likely to change dramatically from site to site: at locations such as the Great Barrier Reef, the islands are larger and freshwater sources may create larger-scale circulation anomalies which require careful attention to properly choose optimal sites for composite construction.

An important distinction here is the inference of ENSO changes using conversions to "instrumental" data [i.e., *Thompson et al.*, 2011; *Stevenson et al.*, 2013] versus those which draw conclusions based on coral records benchmarked to modern $\delta^{18}O$ time series [i.e., *Cobb et al.*, 2003]. The former approach offers the potential for informing improvements to climate model projections, assuming that the uncertainties in the $\delta^{18}O$-ENSO transfer functions can be mitigated. The latter approach is more difficult to apply quantitatively but obviates the need for transfer functions (at the cost of needing to explicitly account for water mass transport). However, even in "like to like" comparisons between modern and fossil coral records, the implicit assumption being made is that the types of mesoscale influences documented here can be considered equivalent during past and present climates. This may be true to first order, but given the potential for interactions between the mean state, ENSO, and the types of processes shown to generate mesoscale variability here, further testing of this hypothesis may be warranted.

A further illustration of the mesoscale impacts on interannual coral $\delta^{18}O$ variability is shown in Figure 14e, where the 2–7 year band-passed coral $\delta^{18}O$ at Palmyra has been computed for PAC and LI. As for the time series in Figure 6, differences are most pronounced during La Niña episodes, consistent with the preferential occurrence of TIWs at these times. The overall changes in band-pass-filtered variance are a 13% reduction at Christmas and a 15% enhancement at Palmyra (not pictured); these changes are a significant fraction of the variance increase documented over the last millennium using Line Islands fossil corals [*Cobb et al.*, 2013]. This indicates that correctly accounting for mesoscale influences on reconstructed ENSO variance might alter interpretations of Holocene ENSO history, which is clearly a task well suited to evaluation with isoROMS given the demonstrated success documented here.

6. Conclusions

This study presents a newly developed isotope-enabled Regional Ocean Modeling System or isoROMS, which is capable of directly simulating the controls on coral oxygen isotopic composition near reefs used for climate reconstruction. The use of ROMS as the framework for this study allows multiscale simulation of the relevant dynamics in a realistic framework free from the biases which affect general circulation models, making it ideal for developing new δ^{18}O-based transfer functions for ENSO.

The present simulations are based on two isoROMS experiments extending from 1979 to 2009, covering the satellite era where interannual precipitation data are available. When forced with heat fluxes, wind, and precipitation fields from CORE2, boundary conditions from GECCO2 and the time-mean seawater isotope product of *LeGrande and Schmidt* [2006], and precipitation δ^{18}O fields from the isotope-enabled CAM5, isoROMS is able to simulate the twentieth century climate fairly accurately. Representation of temperature is quite good, both in the NINO3.4 index region and at grid points close to sites used previously for δ^{18}O collection. Salinity is not as well simulated but agrees with GECCO2 to within the limits of uncertainty. The lower skill in salinity simulation suggests that three-dimensional water mass transport processes (including atmospheric freshwater exchanges) are not depicted as well as temperature, which has consequences for advected trace constituents.

Downscaling to 10 km resolution is performed from the parent PAC simulation, to assess the role of small-scale dynamics on conditions near the Line Islands chain. Resolution is found to strongly influence the magnitude of cold surface temperature extremes at Palmyra, due primarily to the improved simulation of tropical instability waves. TIW activity is known to be best resolved at grid sizes 10 km or smaller [*Marchesiello et al.*, 2011], and at Palmyra this creates excursions of over 0.5°C during certain boreal winter/La Niña periods. Some influence of TIW activity on salinity and seawater δ^{18}O also exists, but these effects are smaller than the temperature signal. A slight enhancement of El Niño SST anomalies in the LI simulation is also seen at Palmyra, most likely due to enhanced NECC transport over the shallower bathymetry.

At Christmas Island, the TIW-related surface temperature gradients tend to be smaller than at Palmyra. However, TIW influences remain visible, and the interaction of fronts with island topography is shown to disrupt the submesoscale field sufficiently to create SST offsets of 0.5 to 1°C between the northern and southern shores. This suggests that some portion of the known intercoral δ^{18}O differences documented at Christmas could arise from physical oceanographic effects and points to the importance of characterizing this variability, both when combining records from a single site and when comparing δ^{18}O variance across islands.

This work has important implications for constructing transfer functions to infer ENSO variance from coral δ^{18}O: the relation between salinity and seawater δ^{18}O becomes less well constrained at higher resolution, possibly from small-scale processes influencing the two quantities differently. At Palmyra, extreme El Niño and La Niña events also lead to larger coral δ^{18}O excursions at higher resolution, flattening the slope of the NINO3.4 SSTA: coral δ^{18}O relationship and altering the resulting ENSO variance estimate. In light of the success of the isoROMS model, improved methods for conversion between coral δ^{18}O and other oceanic properties which account for three-dimensional water mass transport become possible and offer a path toward enhanced understanding of past ocean circulation.

Appendix A: Derivation of the Isotopic Ratio Budget

For ease of interpretation, budgets of the isotopic ratio in seawater are derived, in addition to the budget for $H_2^{16}O$. Here the isotopic ratio R is expressed as

$$R = \frac{H_2^{18}O}{H_2^{16}O} \tag{A1}$$

By the quotient rule,

$$\frac{\partial R}{\partial t} = \frac{1}{H_2^{16}O}\frac{\partial H_2^{18}O}{\partial t} - \frac{R}{H_2^{16}O}\frac{\partial H_2^{16}O}{\partial t} \tag{A2}$$

Substituting the budget equation (8) and its $H_2^{16}O$ equivalent into (A2) yields an isotopic ratio surface flux

$$\Phi_R = \frac{1}{H_2^{16}O}\left(\Phi_{H_2^{18}O} - \frac{H_2^{18}O}{H_2^{16}O}\Phi_{H_2^{16}O}\right) \tag{A3}$$

and three-dimensional advection

$$\frac{1}{H_2^{16}O}\left(-\vec{v}\cdot\nabla H_2^{18}O+\frac{H_2^{18}O}{H_2^{16}O}\vec{v}\cdot\nabla H_2^{16}O\right) \tag{A4}$$

The vertical diffusive/dissipative term is computed as the difference between (A3) + (A4) and $\frac{\partial R}{\partial t}$.

In the main text, all budgets are reported in units of ‰/month, where the conversion between the isotopologue mass ratio and ‰ is accomplished via

$$\frac{\partial \delta^{18}O}{\partial t}=\frac{1000}{R_{std}}\frac{\partial R}{\partial t} \tag{A5}$$

where R_{std} is the ratio of $H_2^{18}O$ to $H_2^{16}O$ in Vienna Standard Mean Ocean Water or 2005.2 ppm.

Acknowledgments
This work is supported by an NSF Ocean Sciences postdoctoral fellowship to S.S., OCE-1323104. D.N. and J.N. were supported by the NSF Paleoclimate (AGS-1049104) and Climate and Large-scale Dynamics (AGS-0955841) programs. Computing resources were provided by the Climate Simulation Laboratory at NCAR's Computational and Information Systems Laboratory (CISL) sponsored by the National Science Foundation and other agencies. NOAA_OI_SST_V2 data are provided by the NOAA/OAR/ESRL PSD, Boulder, CO, USA from their website at http://www.esrl.noaa.gov/psd/. Data from the isoROMS simulations presented here are available on the Earth System Grid Gateway at the National Center for Atmospheric Research: http://www.earthsystemgrid.org.

References

Alibert, C., and M. T. McCulloch (1997), Strontium/calcium ratios in modern porites corals from the Great Barrier Reef as a proxy for sea surface temperature: Calibration of the thermometer and monitoring of ENSO, *Paleoceanography*, *12*(3), 345–363.
An, S.-I. (2008), Interannual variations of the tropical ocean instability wave and ENSO, *J. Clim.*, *21*, 3680–3686.
An, S.-I., and F.-F. Jin (2004), Nonlinearity and asymmetry of ENSO, *J. Clim.*, *17*, 2399–2412.
Barnier, B., L. Siefridt, and P. Marchesiello (1995), Thermal forcing for a global ocean circulation model using a three-year climatology of ECMWF analyses, *J. Mar. Syst.*, *6*, 363–380.
Beck, J. W., R. L. Edwards, E. Ito, F. W. Taylor, J. Recy, F. Rougerie, P. Joannot, and C. Henin (1992), Sea-surface temperature from coral skeletal strontium/calcium ratios, *Science*, *257*(5070), 644–647, doi:10.1126/science.257.5070.644.
Bellenger, H., E. Guilyardi, J. Leloup, M. Lengaigne, and J. Vialard (2013), ENSO representation in climate models: From CMIP3 to CMIP5, *Clim. Dyn.*, *42*, 1999–2018, doi:10.1007/s00382-013-1783-z.
Cahyarini, S. Y., M. Pfeiffer, O. Timm, W.-C. Dullo, and D. G. Schonberg (2008), Reconstructing seawater $\delta^{18}O$ from paired coral $\delta^{18}O$ and Sr/Ca ratios: Methods, error analyses and problems, with examples from Tahiti (French Polynesia) and Timor (Indonesia), *Geochim. Cosmochim. Acta*, *72*, 2841–2853.
Cai, W., et al. (2012), More extreme swings of the South Pacific convergence zone due to greenhouse warming, *Nature*, *488*, 365–369, doi:10.1038/nature11358.
Chapman, D. C. (1985), Numerical treatment of cross-shelf open boundaries in a barotropic coastal ocean model, *J. Phys. Oceanogr.*, *15*, 1060–1075.
Chelton, D. B., R. A. deSzoeke, M. G. Schlax, K. E. I. Naggar, and N. Siwertz (1998), Geographical variability of the first baroclinic Rossby radius of deformation, *J. Phys. Oceanogr.*, *28*, 433–460.
Cobb, K., C. Charles, H. Cheng, and R. Edwards (2003), El Niño/Southern Oscillation and tropical Pacific climate during the last millennium, *Nature*, *424*, 271–276.
Cobb, K., C. Charles, and D. Hunter (2001), A central tropical Pacific coral demonstrates Pacific, Indian, and Atlantic decadal climate connections, *Geophys. Res. Lett.*, *28*, 2209–2212.
Cobb, K., C. D. Charles, H. Cheng, R. L. Edwards, H. R. Sayani, and N. Westphal (2013), Highly variable El Niño-Southern Oscillation throughout the Holocene, *Science*, *339*, 67–70, doi:10.1126/science.1228246.
Cole, J. E., R. G. Fairbanks, and G. T. Shen (1993), Recent variability in the Southern Oscillation: Isotopic results from a Tarawa Atoll coral, *Science*, *260*, 1790–1793.
Conroy, J. L., K. M. Cobb, J. Lynch-Stieglitz, and P. J. Polissar (2014), Constraints on the salinity-oxygen isotope relationship in the central tropical Pacific Ocean, *Mar. Chem.*, *161*, 26–33, doi:10.1016/j.marchem.2014.02.001.
Craig, H., and L. I. Gordon (1965), Deuterium and oxygen-18 variations in the ocean and marine atmosphere, *Proc. Spoleto Conf. on Nuclear Geology, Stable Isotopes in Oceanic Studies and Paleotemperatures, Pisa, Italy, Consiglio Nazionale delle Ricerche, Laboratorio di Geologia Nucleare, 9130*.
Dassie, E. P., B. K. Linsley, T. Correge, H. C. Wu, G. M. Lemley, S. Howe, and G. Cabioch (2014), A Fiji multi-coral $\delta^{18}O$ composite approach to obtaining a more accurate reconstruction of the last two-centuries of the ocean-climate variability in the South Pacific Convergence Zone region, *Paleoceanography*, *29*, 1196–1213, doi:10.1002/2013PA002591.
Delcroix, T., G. Alory, S. Cravatte, T. Correge, and M. J. McPhaden (2011), A gridded sea surface salinity data set for the tropical Pacific with sample applications (1950–2008), *Deep Sea Res.*, *58*, 38–48.
DeLong, K., T. M. Quinn, F. W. Taylor, K. Lin, and C.-C. Shen (2012), Sea surface temperature variability in the southwest tropical Pacific since AD 1649, *Nat. Clim. Change*, *2*, 799–804.
DeLong, K., T. M. Quinn, F. W. Taylor, C.-C. Shen, and K. Lin (2013), Improving coral-base paleoclimate reconstructions by replicating 350 years of coral Sr/Ca variations, *Palaeogeogr. Palaeoclimatol. Palaeoecol.*, *373*, 6–24.
Durack, P. J., S. E. Wijffels, and R. J. Matear (2012), Ocean salinities reveal strong global water cycle intensification during 1950 to 2000, *Science*, *336*(455), 455–458, doi:10.1126/science.1212222.
Epstein, S., R. Buchsbaum, H. A. Lowenstam, and H. C. Urey (1953), Revised carbonate/water isotopic temperature scale, *Geol. Soc. Am. Bull.*, *64*(11), 1315–1326, doi:10.1130/0016-7606(1953)64[1315:RCITS]2.0.CO;2.
Evans, M. N., A. Kaplan, and M. A. Cane (1998), Optimal sites for coral-based reconstructions of global sea surface temperature, *Paleoceanography*, *13*(5), 502–516.
Evans, M. N., R. G. Fairbanks, and J. L. Rubenstone (1999), The thermal oceanographic signal of El Niño reconstructed from a Kiritimati Island coral, *J. Geophys. Res.*, *104*(C6), 13,409–13,421.
Evans, M. N., A. Kaplan, and M. A. Cane (2000), Intercomparison of coral oxygen isotope data and historical sea surface temperature (SST): Potential for coral-based SST field reconstructions, *Paleoceanography*, *15*(5), 551–562.
Fairbanks, R., M. Evans, J. Rubenstone, R. Mortlock, K. Broad, M. Moore, and C. Charles (1997), Evaluating climate indices and their geochemical proxies measured in corals, *Coral Reefs*, *16*, S93–S100.

Flather, R. A. (1976), A tidal model of the northwest European continental shelf, *Mem. Soc. R. Sci. Liege*, *6*, 141–164.
Folland, C. K., J. A. Renwick, M. J. Salinger, and A. B. Mullan (2002), Relative influences of the Interdecadal Pacific oscillation and ENSO on the South Pacific Convergence Zone, *Geophys. Res. Lett.*, *29*(13), 1643, doi:10.1029/2001GL014201.
Gagan, M., G. Dunbar, and A. Suzuki (2012), The effect of skeletal mass accumulation in Porites on coral Sr/Ca and δ^{18}O paleothermometry, *Paleoceanography*, *27*, PA1203, doi:10.1029/2011PA002215.
Gorman, M., et al. (2012), A coral-based reconstruction of sea surface salinity at Sabine Bank, Vanuatu from 1842 to 2007 CE, *Paleoceanography*, *27*, PA3226, doi:10.1029/2012PA002302.
Guilderson, T. P., and D. P. Schrag (1999), Reliability of coral isotope records from the western Pacific warm pool: A comparison using age-optimized records, *Paleoceanography*, *14*, 457–464.
Guilyardi, E., A. Wittenberg, A. Fedorov, M. Collins, C. Wang, A. Capotondi, G. Jan van Oldenborgh, and T. Stockdale (2009), Understanding El Niño in ocean-atmosphere general circulation models: Progress and challenges, *Bull. Am. Meteorol. Soc.*, *90*, 325–340.
Hamann, I. M., G. W. Boehlert, and C. D. Wilson (2004), Effects of steep topography on the flow and stratification near Palmyra Atoll, *Ocean Dyn.*, *54*, 460–473.
Haney, R. L. (1971), Surface thermal boundary conditions for ocean circulation models, *J. Phys. Oceanogr.*, *1*, 241–248.
Hoffmann, G., M. Werner, and M. Heimann (1998), Water isotope module of the ECHAM atmospheric general circulation model: A study on timescales from days to several years, *J. Geophys. Res.*, *103*(D14), 16,871–16,896.
Hoskins, B., and K. Karoly (1981), The steady response of a spherical atmosphere to thermal and orographic forcing, *J. Atmos. Sci.*, *38*, 1179–1196.
Jouzel, J., G. L. Russell, R. J. Suozzo, R. D. Koster, J. W. C. White, and W. S. Broecker (1987), Simulations of the HDO and $H_2{}^{18}O$ atmospheric cycles using the NASA GISS general circulation model: The seasonal cycle for present-day conditions, *J. Geophys. Res.*, *92*(D12), 14,739–14,760, doi:10.1029/JD092iD12p14739.
Kennan, S. C., and P. J. Flament (2000), Observations of a tropical instability vortex, *J. Phys. Oceanogr.*, *30*(9), 2277–2301.
Kohl, A. (2014), Evaluation of the GECCO2 ocean synthesis: Transports of volume, heat and freshwater in the Atlantic, *Q. J. R. Meteorol. Soc.*, *141*, 166–181, doi:10.1002/qj.2347.
Large, W. G., and S. G. Yeager (2008), The global climatology of an interannually varying air-sea flux data set, *Clim. Dyn.*, *33*, 341–364.
Legeckis, R. (1977), Long waves in the eastern equatorial Pacific Ocean: A view from a geostationary satellite, *Science*, *197*, 1179–1181.
LeGrande, A. N., and G. A. Schmidt (2006), Global gridded data set of the oxygen isotopic composition in seawater, *Geophys. Res. Lett.*, *33*, L12604, doi:10.1029/2006GL026011.
Linsley, B., A. Kaplan, Y. Gouriou, J. Salinger, P. deMenocal, G. Wellington, and S. Howe (2006), Tracking the extent of the South Pacific Convergence Zone since the early 1600s, *Geochem. Geophys. Geosyst.*, *7*, Q05003, doi:10.1029/2005GC001115.
Linsley, B. K., R. B. Dunbar, G. M. Wellington, and D. A. Mucciarone (1994), A coral-based reconstruction of Intertropical Convergence Zone variability over Central America since 1707, *J. Geophys. Res.*, *99*, 9977–9994.
Lough, J. M. (2010), Climate records from corals, *Wiley Intersci. Rev.*, *1*, 318–331.
Lyman, J. M., G. C. Johnson, and W. S. Kessler (2007), Distinct 17- and 33-day tropical instability waves in subsurface observations, *J. Phys. Oceanogr.*, *37*, 855–872.
Marchesiello, P., X. Capet, C. Menkes, and S. C. Kennan (2011), Submesoscale dynamics in tropical instability waves, *Ocean Modell.*, *39*, 31–46, doi:10.1016/j.ocemod.2011.04.011.
Matthews, D., B. Powell, and R. Milliff (2011), Dominant spatial variability scales from observations around the Hawaiian Islands, *Deep Sea Res. Part I*, *58*(10), 979–987.
McGregor, H. V., M. J. Fischer, M. K. Gagan, D. Fink, S. J. Phipps, H. Wong, and C. D. Woodroffe (2013), A weak El Niño-Southern Oscillation with delayed seasonal growth around 4,300 years ago, *Nat. Geosci.*, *6*, 949–953, doi:10.1038/ngeo1936.
McGregor, H. V., M. J. Fischer, M. K. Gagan, D. Fink, and C. D. Woodroffe (2011), Environmental control of the oxygen isotope composition of Porites coral microatolls, *Geochim. Cosmochim. Acta*, *75*, 3930–3944.
McPhaden, M., et al. (1998), The tropical ocean-global atmosphere observing system: A decade of progress, *J. Geophys. Res.*, *103*, 14,169–14,240.
McPhaden, M. J., and S. P. Hayes (1990), Variability in the eastern equatorial Pacific Ocean during 1986–1988, *J. Geophys. Res.*, *95*(C8), 13,195–13,208, doi:10.1029/JC095iC08p13195.
Mellor, G. L., and T. Yamada (1982), Development of a turbulence closure model for geophysical fluid problems, *Rev. Geophys.*, *20*(4), 851–875, doi:10.1029/RG020i004p00851.
Merlivat, L., and J. Jouzel (1979), Global climatic interpretation of the deuterium-oxygen 18 relationship for precipitation, *J. Geophys. Res.*, *84*(C8), 5029–5033.
Noone, D., and I. Simmonds (2002), Associations between delta O-18 of water and climate parameters in a simulation of atmospheric circulation for 1979-95, *J. Clim.*, *15*, 3150–3169.
Noone, D. C. (2006), Isotopic composition of water vapor modeled by constraining global climate simulations with reanalyses, in *Research Activities in Atmospheric and Oceanic Modelling*, edited by J. Cote, pp. 2–37, Rep. 35, World Meteorological Organization, Geneva, Switzerland.
Noone, D., and C. Sturm (2010), Comprehensive dynamical models of global and regional water isotope distributions, in *Isoscapes*, edited by J. B., West et al., pp. 195–219, Springer, Netherlands.
Nurhati, I., K. Cobb, C. Charles, and R. Dunbar (2009), Late 20th century warming and freshening in the central tropical Pacific, *Geophys. Res. Lett.*, *36*, L21606, doi:10.1029/2009GL040270.
Nurhati, I. S., K. M. Cobb, and E. Di Lorenzo (2011), Decadal-scale SST and salinity variations in the central tropical Pacific: Signatures of natural and anthropogenic climate change, *J. Clim.*, *24*, 3294–3308.
Nusbaumer, J., T. Wong, and D. C. Noone (2014), The impact of differing land surface models and water isotopic parameterizations on the distribution of water isotopes in a coupled atmosphere-land global climate model, *AGU Fall Meeting, San Francisco, Calif*.
Quinn, T. M., T. J. Crowley, F. W. Taylor, C. Henin, P. Joannot, and Y. Join (1998), A multicentury stable isotope record from a New Caledonia coral: Interannual and decadal SST variability in the southwest Pacific since 1657, *Paleoceanography*, *13*, 412–426.
Rayner, N. A., D. E. Parker, E. B. Horton, C. K. Folland, L. V. Alexander, D. P. Rowell, E. C. Kent, and A. Kaplan (2003), Global analyses of sea surface temperature, sea ice, and night marine air temperature since the late nineteenth century, *J. Geophys. Res.*, *108*(D14), 4407, doi:10.1029/2002JD002670.
Reynolds, R., N. Rayner, T. Smith, D. Stokes, and W. Wang (2002), An improved in situ and satellite SST analysis for climate, *J. Clim.*, *15*, 1609–1625.
Russon, T., A. W. Tudhope, G. C. Hegerl, M. Collins, and J. Tindall (2013), Inter-annual tropical Pacific climate variability in an isotope-enabled CGCM: Implications for interpreting coral stable oxygen isotope records of ENSO, *Clim. Past*, *9*, 1543–1557.

Shchepetkin, A., and J. McWilliams (2005), The Regional Ocean Modeling System (ROMS): A split-explicit, free-surface, topography-following coordinates ocean model, *Ocean Modell.*, *9*(4), 347–404.

Smith, T., R. W. Reynolds, T. C. Peterson, and J. Lawrimore (2008), Improvements to NOAA's historical merged land-ocean surface temperature analysis (1880–2006), *J. Clim.*, *21*, 2283–2296.

Souza, J., B. Powell, A. Castillo-Trujillo, and P. Flament (2015), The vorticity balance of the ocean surface in Hawaii from a regional reanalysis, *J. Phys. Oceanogr.*, *45*, 424–440, doi:10.1175/JPO-D-14-0074.1.

Stephens, G. L., et al. (2010), Dreary state of precipitation in global models, *J. Geophys. Res.*, *115*, D24211, doi:10.1029/2010JD014532.

Stevenson, S., B. Fox-Kemper, M. Jochum, R. Neale, C. Deser, and G. Meehl (2012), Will there be a significant change to El Niño in the 21st century?, *J. Clim.*, *25*, 2129–2145, doi:10.1175/JCLI-D-11-00252.1.

Stevenson, S., B. Fox-Kemper, M. Jochum, B. Rajagopalan, and S. Yeager (2010), Model ENSO validation using wavelet probability analysis, *J. Clim.*, *23*, 5540–5547.

Stevenson, S., H. V. McGregor, S. Phipps, and B. Fox-Kemper (2013), Quantifying errors in coral-based ENSO estimates: Towards improved forward modeling of δ^{18}O, *Paleoceanography*, *28*, 633–649, doi:10.1002/palo.20059.

Thompson, D. M., T. R. Ault, M. N. Evans, J. E. Cole, and J. Emile-Geay (2011), Comparison of observed and simulated tropical climate trends using a forward model of coral δ^{18}O, *Geophys. Res. Lett.*, *38*, L14706, doi:10.1029/2011GL048224.

Tudhope, A. W., et al. (2001), Variability in the El Niño/Southern Oscillation through a glacial-interglacial cycle, *Science*, *291*, 1511–1517.

Urban, F., J. Cole, and J. Overpeck (2000), Influence of mean climate change on climate variability from a 155- year tropical Pacific coral record, *Nature*, *407*, 989–993.

Wittenberg, A. T. (2009), Are historical records sufficient to constrain ENSO simulations?, *Geophys. Res. Lett.*, *36*, L12702, doi:10.1029/2009GL038710.

Woodroffe, C. D., M. R. Beech, and M. K. Gagan (2003), Mid-late Holocene El Niño variability in the equatorial Pacific from coral microatolls, *Geophys. Res. Lett.*, *30*(7), 1358, doi:10.1029/2002GL015868.

Woodroffe, C. D., and M. K. Gagan (2000), Coral microatolls from the central Pacific record late Holocene El Niño, *Geophys. Res. Lett.*, *27*, 1511–1514.

Yu, J.-Y., and W. Liu (2003), A linear relationship between ENSO intensity and tropical instability wave activity in the eastern Pacific Ocean, *Geophys. Res. Lett.*, *30*(14), 1735, doi:10.1029/2003GL01716.